International Journal of Mechanical Sciences 231 (2022) 107565

Contents lists available at ScienceDirect

International Journal of Mechanical Sciences

journal homepage: www.elsevier.com/locate/ijmecsci

Energy harvesting from thermally induced vibrations of antenna panels

Dewen Yu [a,b], Yaowen Yang [b,*], Guobiao Hu [b,*], Yifan Zhou [c], Jun Hong [a]

[a] Key Laboratory of Education Ministry for Modern Design and Rotor-Bearing System, School of Mechanical Engineering, Xi'an Jiaotong University, Xianning West Road, Xi'an 710049, China
[b] School of Civil and Environmental Engineering, Nanyang Technological University, 50 Nanyang Avenue, Singapore 639798, Singapore
[c] State Key Laboratory for Strength and Vibration of Mechanical Structures, International Center for Applied Mechanics, School of Aerospace Engineering, Xi'an Jiaotong University, Xianning West Road, Xi'an 710049, China

ARTICLE INFO

Keywords:
Energy harvesting
Thermoelastic formulation
Piezoelectric transducer
Thermally induced vibration

ABSTRACT

Though vibration energy harvesting technology has been extensively explored in the past decades, harnessing energy from thermally induced vibration has been rarely investigated. This study, for the first time, proposes a piezoelectric energy harvester (PEH) excited by time-varying thermal loading in outer space to power wireless electronics in antenna panels of satellites. A novel thermal-mechanical-electrical coupling model is developed to accurately predict the dynamic response of the system. Firstly, based on the comprehensive analysis of spatial heat fluxes, the transient thermal conduction equations are derived via the variational principle. Subsequently, different from conventional incremental finite elements, the thermoelasticity of the panel is characterized by the absolute nodal formulation. Taking advantage of invariant matrices, an enhanced mathematical model is constructed to improve the computational efficiency of the thermoelastic forces and their Jacobian matrices. Furthermore, an electromechanically-coupled analytical model is put forward for the PEH installed on the antenna panel. Finally, an integrated computational framework is established to iteratively solve the multi-physics coupled problem with second-order accuracy. A corresponding finite element model is also built for verification. The effectiveness and efficiency of the developed multi-physics model are demonstrated through a comparison with the simulation results. In particular, the proposed analytical model not only considers the bidirectional interaction between the elastic deformation and heat absorption, but also incorporates the coupling relationship between the piezoelectric effect and structural vibration. Moreover, the investigation results provide pivotal insights into the design of the energy harvesting system excited by thermally induced vibration.

1. Introduction

With the increasing demand for high-resolution satellites, intelligent sensors and actuators are implemented in antennas to realize deformation monitoring and dynamic adjustment [1–3]. Such distributed control systems can improve the shape accuracy of panels without human intervention [4–6]. Given the harsh service conditions in outer space, wires and associated connectors have a high risk of failure [7,8], thus wireless devices are preferred. Solar batteries are currently the most frequently used energy source for spacecraft equipment. However, solar energy is not always the optimal choice for those scattered low-power wireless electronics [9] because of the limited performance adaptability and high allocation cost of solar batteries [10]. In this context, other alternative solutions are desired to enable high design flexibility [11,12], which is also critical for high-performance autonomous remote devices [13].

In addition to the solar energy in outer space, the vibration energy of antennas could also be harnessed and converted into electricity to provide a potential power supply solution. According to the literature, there are four common mechanical-to-electrical energy conversion mechanisms [14], namely electromagnetic, electrostatic, triboelectric, and piezoelectric transductions [15]. Electromagnetic transductions make use of external mechanical excitation to change the magnetic flux across the coil [16], and two strategies can be derived from the principle [17]: either creating a relative movement between the magnet and coil, or applying self-actuated ferromagnetic materials. However, the introduced magnetic field may deteriorate the polarization performance of antennas [18] so that the above approaches of electromagnetic transduction are not applicable. Electrostatic harvesters take the form of variable capacitors, whose capacitance varies with the displacement of

---

* Corresponding authors.
E-mail addresses: cywyang@ntu.edu.sg (Y. Yang), guobiao.hu@ntu.edu.sg (G. Hu).

https://doi.org/10.1016/j.ijmecsci.2022.107565
Received 16 May 2022; Received in revised form 14 July 2022; Accepted 19 July 2022

movable electrodes. Although electrostatic transductions are more competitive in compact size and compatibility to the system, they require external voltage sources to apply potential on electrodes. Moreover, on the condition of off-axis vibrations, the rotation of combs may trigger collisions between the capacitors [19], thereby causing severe damage to the electrostatic harvesters. Triboelectric transductions are based on the periodic separation and contact of two objects with opposite triboelectric properties which create induced charge flow via external loads [20]. However, triboelectric energy harvesters have the deficiencies of low reliability and stretchability [21]. Piezoelectric transductions employ piezoelectric materials to directly convert mechanical strain into electrical potential. Due to the simple architectures and high energy density, piezoelectric transducers are more durable and reliable [22] as compared to the other counterparts. Therefore, using piezoelectric transducers to harness energy from the vibrations of antenna panels is a promising scheme.

Numerous efforts have been devoted to developing diverse piezoelectric energy harvesters (PEHs) in the past two decades. A variety of designs have been proposed based on beams [23], shells [24], and plates [25] for different engineering applications [26–28]. Meanwhile, various theoretical models, ranging from the lumped parameter model [29,30], the Rayleigh–Ritz approximate distributed parameter model [31,32], to the closed-form distributed parameter model [33,34], have been established to predict the dynamic responses of PEHs. Erturk and Inman [35] pointed out that classical lumped models are sometimes oversimplified. In particular, when sophisticated interfaces and boundary conditions are considered, it becomes challenging to obtain the analytical solution to multi-degree-of-freedom systems. To address these issues, electromechanical finite element models have been constructed to predict the electrical power outputs of PEHs [36–38]. These discretized approaches boosted the numerical techniques for characterizing electromechanical behaviors. For example, Yang and Tang [39] derived the system parameters of a piezoelectric cantilever energy harvester via finite element analysis, and obtained a multi-mode equivalent model. In addition to commercial software, customized finite element formulations were also developed to reduce the computational cost. According to the generalized Hamilton's principle, Fattahi and Mirdamadi [40] constructed a finite element discretization model where the strain, displacement and electric potential were decomposed into longitudinal and cross-sectional components. Ramirez et al. [41] presented a one-dimensional nonlinear finite element for modeling three-dimensional rotational energy harvesters, where the electromechanical equilibrium motion equations were derived by following the D'Alembert principle. Ravi and Zilian [42] introduced a monolithic finite element formulation to compute the natural frequencies and the corresponding mode shapes of a PEH. They converted the coupled governing equations into a single integral form with six independent fields. According to the literature review [43,44], most finite element formulations focused only on the electromechanical coupling effect of piezoelectric plates/shells with a static point load. However, cases under distributed and time-varying loads have been rarely investigated.

Like other on-orbit spacecraft, antenna panels suffer from periodic heating and cooling, with the temperature ranging from −70 to 120 ℃ [45]. For instance, the transition between sunlight and shadow regions induces significant temperature changes and time-dependent bending moments [46], leading to structural vibrations of antenna panels [4,47]. In this circumstance, thermally induced vibration analysis becomes the premise of predicting the electromechanical behaviors of PEHs installed on the antenna panels. According to whether the thermal deformation reversely affects heat exchange, existing approaches can be divided into two categories for the response analysis of thermally induced vibration: partially and fully coupled models. Bless et al. [48] investigated the transient thermal response of a flexible panel by adopting the Von Karman strain–displacement formula. Liu and Lu [49] extended the hybrid coordinate formulation to derive the structural deformation of an elastic beam under thermal disturbance. Although the nonlinear geometric effect was considered in [48,49], the actual thermomechanical interaction was overlooked by directly assuming a priori temperature profile on the physical surface. In the rigid-flexible-thermal coupling analysis, Daneshjo and Ramezani [50] developed a mixed finite element formulation to predict the thermoelastic response of composite plates, but the effects of energy dissipation in the mechanical work on the temperature field were not taken into account [51]. Using generalized linear thermoelasticity theories, Kar and Kanoria [52] determined the thermo-elastic interaction due to a step-input of temperature on the boundaries. Wang et al. [53] derived a unified generalized thermoelasticity solution for the transient thermal shock problem within the framework of three thermoelasticity theories. However, most thermoelastic models were constrained to fixed coordinate systems. Liu and Pan [54] employed the floating frame of reference formulation to reveal the rigid-flexible-thermal coupling effect of an orbiting satellite. Taking advantage of the absolute nodal coordinate formulation in describing large deformation, Liu et al. [55] proposed a novel combined approach with the natural coordinate formulation for the dynamic analysis. They also developed an efficient formulation for evaluating the elastic forces and their Jacobians. Later, Shen et al. [56] conducted a coupled thermal–structural analysis for the thermally induced vibration of a thin-walled tubular boom. Based on the absolute nodal coordinate formulation, Cui et al. [57] derived a plate element that could integrate the heat transfer and dynamic analysis via a unified description. In addition, it is worth mentioning that although some low-grade thermal energy harvesting technologies, such as thermoelectric generators [58], have been proposed, they rely on the thermoelectric, pyroelectric, and thermomagnetic effects [59]. In general, piezoelectric energy harvesting from thermally induced vibrations of aerospace structures has yet been discussed in the literature.

As reviewed above, no analytical model is available to predict the dynamic responses of PEHs under thermally induced vibration. This paper, for the first time, proposes to utilize the piezoelectric effect to harness the strain energy from the thermally induced vibration of an antenna in outer space. To tackle this challenge, a novel rigorous theoretical framework is developed to reveal the electro-mechanical-thermal conversion characteristics of the developed PEH. The main novelties and contributions are summarized as follows. (1) Unlike extensively studied thermal energy harvesters that utilize thermoelectric materials and pyroelectric generators, the proposed system converts thermally induced vibration into electricity via the piezoelectric effect. (2) Instead of partially coupled approaches, a complete analytical methodology with the full consideration of interactions is established to model the multi-physics involved dynamic process of harvesting energy from the structural vibration induced by time-varying thermal loads. (3) A novel computational framework for dynamic thermoelastic analysis is developed with the absolute nodal coordinate formulation, not only the thermoelastic forces and corresponding Jacobian matrices are evaluated efficiently, but also the governing equations of the whole system are synchronously solved with second-order accuracy.

The rest of this paper is organized as follows. Section 2 elaborates on the thermal environment of an on-orbit satellite in outer space and derives the transient heat conduction of the antenna panel. Section 3 analyzes the thermoelasticity of the antenna panel with the absolute nodal coordinate formulation. Section 4 presents the electromechanical analysis of the piezoelectric transducer. In Section 5, by taking the electro-mechanical-thermal coupling effect into account, an integrated framework is established to predict the performance of the PEH. Section 6 provides a representative case study for proof-of-concept and to validate the proposed method. Finally, conclusions are outlined in Section 7.

2. Thermal analysis and heat conduction

Antenna panels are subjected to multiple thermal loads in outer space, including solar radiation fluxes, Earth-emitted heat radiation fluxes, Earth-reflected heat radiation fluxes, and surface radiations.

Moreover, the thermal load of the antenna panel varies with time. To characterize the effect of these external heat fluxes on antenna panels, this section will quantify these time-varying thermal loads and develop an analytical model of heat conduction.

2.1. Thermal loading analysis

As depicted in Fig. 1, the heat fluxes change periodically when the antenna moves among the light, twilight, and shadow zones. To reveal the heat conduction process, the external heat fluxes are to be formulated for the antenna panel in orbit.

As shown in Fig. 1, R_s and R_e denote the radii of the Sun and the Earth, respectively. R_{se} denotes the distance between the Sun and the Earth. For convenience, three angles γ_1, γ_2, and γ_3 are defined to describe the attitude of the satellite. According to the geometric relationship, these angles can be derived as:

$$\begin{cases} \gamma_1 = \mathrm{acrsin}\dfrac{R_e}{R_e + H_a} \\ \gamma_2 = \mathrm{acrsin}\dfrac{R_s}{\sqrt{R_{se}^2 + (R_e + H_a)^2 - 2R_{se}(R_e + H_a)\cos\varphi}}, \\ \gamma_3 = \mathrm{acrsin}\dfrac{R_{se}|\sin\varphi|}{\sqrt{R_{se}^2 + (R_e + H_a)^2 - 2R_{se}(R_e + H_a)\cos\varphi}} \end{cases} \tag{1}$$

where H_a is the satellite orbit height, and φ is illustrated in Fig. 1. From the respective of projective geometry, the position of the satellite can be determined by the following criteria: (1) if $\gamma_3 \geq \gamma_1 + \gamma_2$, the satellite is in the light zone; (2) if $\gamma_3 - \gamma_2 < \gamma_1 < \gamma_2 + \gamma_3$, the satellite enters the twilight zone; (3) if $\gamma_1 \geq \gamma_2 + \gamma_3$, the satellite goes into the shadow zone.

With the modification of angle factors in heat transfer [47], the solar radiation flux q_s absorbed by the panel is formulated as:

$$q_s = \alpha_m S_0 \psi_1, \tag{2}$$

where α_m represents the solar absorptivity of the antenna panel, the solar heat flux S_0 is approximately 1350 W/m^2, and the albedo view factor ψ_1 can be calculated by:

$$\psi_1 = f(t)\cos\alpha_\theta, \tag{3}$$

where α_θ represents the incident angle between the sunlight and the normal vector of the antenna surface, and $f(t)$ is associated with the antenna attitude so that it is a function of time t. In detail, we have [60]:

$$f(t) = \begin{cases} 0, & \textit{in shadowzone} \\ 1 - \left(\dfrac{\gamma_1}{\gamma_2}\right)^2 \left[\dfrac{\chi_1}{\pi} - \dfrac{\sin(2\chi_1)}{2\pi}\right] + \left[\dfrac{\chi_2}{\pi} - \dfrac{\sin(2\chi_2)}{2\pi}\right], & \textit{in twilightzone}\,. \\ 1, & \textit{in lightzone} \end{cases} \tag{4}$$

where the intermediate variables χ_1 and χ_2 are represented as:

$$\chi_1 = \arccos\left(\frac{\gamma_3^2 + \gamma_1^2 - \gamma_2^2}{2\gamma_3\gamma_1}\right), \quad \chi_2 = \arccos\left(\frac{\gamma_3^2 + \gamma_2^2 - \gamma_1^2}{2\gamma_3\gamma_2}\right). \tag{5}$$

The Earth-emitted radiation q_e absorbed by the panel is determined by:

$$q_e = \alpha_e S_e \psi_2. \tag{6}$$

where α_e is the absorptivity of Earth-emitted radiation, and the heat flux of Earth-emitted radiation S_e is 237 W/m^2. The view factor ψ_2 depends on the spatial geometric relation between the panel surface and the Earth, which is expressed as:

$$\psi_2 = \frac{1}{\pi}\int_\varphi\int_\theta (\cos\theta\cos\beta + \sin\theta\sin\beta\cos\varphi)\sin\theta d\theta d\varphi. \tag{7}$$

Here, the spherical coordinate frame (θ, φ) is developed for describing the surface of the Earth as shown in Fig. 2, and β represents the angle between the normal vector of the panel and the connecting line from the Earth to the satellite. Due to the symmetry of the Earth, the

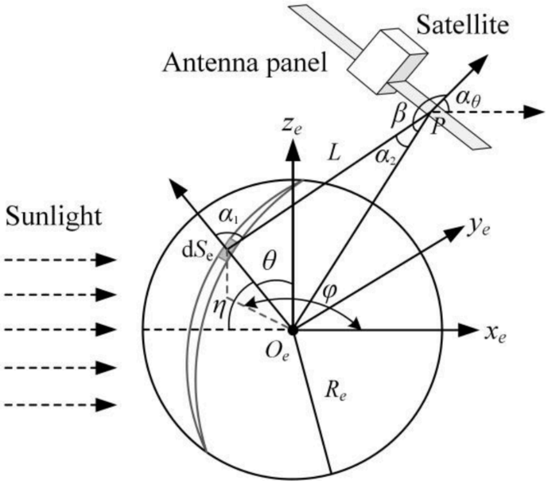

Fig. 2. *Earth-reflected heat radiation flux*. The heat flux reflected by the Earth varies with the location on the Earth surface. The total Earth-reflected heat flux absorbed by the antenna panel should be integrated over the whole surface. For convenience, a spherical coordinate frame (θ, φ) is developed to describe the surface of the Earth. The point P is located at the antenna panel. L is the length of the connecting line from the point P to the surface. α_1 is the angle between the connecting line and the normal vector of the surface. α_2 is the angle between the connecting line and PO_e. β represents the angle between PO_e and the normal vector of the panel. α_θ is the angle between the sunlight and the normal vector of the panel.

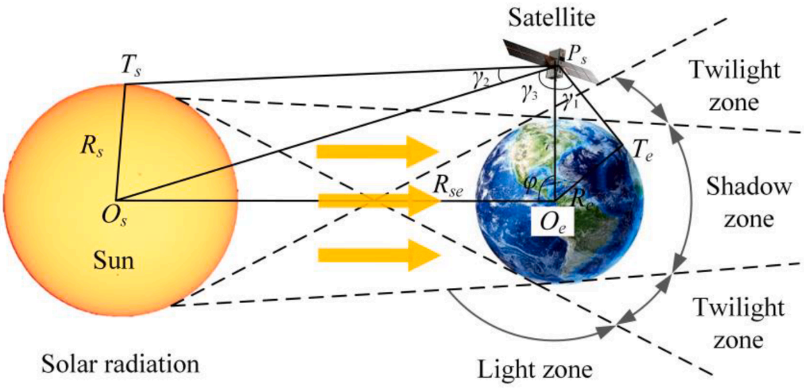

Fig. 1. *Schematic of the thermal environment of an on-orbit satellite*. The satellite periodically travels through the light, twilight, and shadow zones. R_s and R_e are the radii of the Sun and the Earth, respectively. The distance between the Sun and the Earth is denoted by R_{se}. The point P_s represent the barycenter of the satellite. P_sT_s is the tangent line between the satellite and the Sun, while P_sT_e is the tangent line between the satellite and the Earth. φ is the angle between the lines O_eO_s and O_eP_s; γ_1 is the angle between the lines P_sT_e and P_sO_e; γ_2 is the angle between the lines P_sT_s and P_sO_s; and γ_3 is the angle between the lines P_sO_e and P_sO_s.

above integral is only related to β and the orbital height H_a, and it can be calculated as follows [61]:

$$\psi_2 = \begin{cases} K^2\cos\beta, & 0 \le \beta \le \operatorname{acos} K \\ K^2\cos\beta + b, & \operatorname{acos} K < \beta < \pi - \operatorname{acos} K \\ 0, & \pi - \operatorname{acos} K \le \beta \le \pi \end{cases}. \tag{8}$$

The geometric variables K and b are given by:

$$K = \frac{R_e}{R_e + H_a},\ b = \frac{1}{\pi}\left(\frac{\pi}{2} - \sqrt{1-K^2}\sqrt{K^2 - \cos^2\beta} - \operatorname{asin}\frac{\sqrt{1-K^2}}{\sin\beta} - K^2\cos\beta\ \operatorname{acos}\frac{\sqrt{1-K^2}}{K\tan\beta}\right). \tag{9}$$

As depicted in Fig. 2, the Earth-reflected radiation q_r received by the panel is formulated as:

$$q_r = \alpha_m \mathrm{S}_0 \rho_e \psi_3, \tag{10}$$

where ρ_e is the fraction of solar radiation reflected by the Earth, and the thermal coefficient ψ_3 is calculated by:

$$\psi_3 = \int_\varphi \int_\theta \frac{\cos\psi_{31}\cos\psi_{32}\cos\psi_{33}}{\pi L^2} R_e^2 \sin\theta d\theta d\varphi. \tag{11}$$

In particular, ψ_{31}, ψ_{32} and ψ_{33} satisfy the following expressions [54]:

$$\begin{cases} \cos\psi_{31} = \begin{cases} \cos\eta, & 0 \le \eta \le \pi/2 \\ 0, & \pi/2 < \eta \le \pi \end{cases} \\ \cos\psi_{32} = \begin{cases} \cos\alpha_1, & 0 \le \alpha_1 \le \pi/2 \\ 0, & \pi/2 < \alpha_1 \le \pi \end{cases} \\ \cos\psi_{33} = \begin{cases} \cos\alpha_2, & 0 \le \alpha_2 \le \pi/2 \\ 0, & \pi/2 < \alpha_2 \le \pi \end{cases} \end{cases}. \tag{12}$$

The geometric relationships among θ, φ, η, α_1 and α_2 are given by:

$$\begin{cases} \cos\eta = \cos\theta\cos\phi + \sin\theta\sin\phi\cos\phi \\ \cos\alpha_1 = \dfrac{R_e + H_a}{L}\left(\cos\theta - \dfrac{R_e}{R_e + H_a}\right) \\ \cos\alpha_2 = \dfrac{R_e}{LK}((1 - K\cos\theta)\cos\beta + K\sin\theta\sin\beta\cos\phi) \end{cases}, \tag{13}$$

where the distance L is expressed as:

$$L = \sqrt{R_e^2 + (R_e + H_a)^2 - 2R_e(R_e + H_a)\cos\theta}. \tag{14}$$

In addition to these heat fluxes, the antenna panel itself also emits radiation into outer space. Note that the temperature of the upper surface of the antenna panel is generally different from that its lower surface, their radiations of the upper and lower surfaces q_r^u and q_r^l are expressed as:

$$q_r^u = \varsigma_p \sigma_p (T_u - T_c)^4, \quad q_r^l = \varsigma_p \sigma_p (T_l - T_c)^4, \tag{15}$$

where ς_p denotes the emissivity of the panel surface, and σ_p is the Stefan–Boltzmann constant that equals 5.67×10^{-8} W/(m^2 K^4). T_u and T_l are the temperatures of the upper and lower surfaces, respectively. T_c is the temperature of the outer space.

2.2. Formulation of heat conduction

According to the Fourier's law and three boundary conditions, the transient temperature field of the antenna panel takes the following form:

$$\begin{aligned} &\int_{V_a} \rho_a c \delta T \frac{\partial T}{\partial t} dV_a - \int_{V_a} \rho_a \delta T Q_p dV_a - \int_{S_a} \delta T q^u dS_a - \int_{S_a} \delta T q^l dS_a - \int_{S_a} \delta T h_T (T_c - T) dS_a - \\ &\int_{V_a} \left[\delta\left(\frac{\partial T}{\partial x}\right)\left(k_x \frac{\partial T}{\partial x}\right) + \delta\left(\frac{\partial T}{\partial y}\right)\left(k_y \frac{\partial T}{\partial y}\right) + \delta\left(\frac{\partial T}{\partial z}\right)\left(k_z \frac{\partial T}{\partial z}\right)\right] dV_a = 0 \end{aligned}, \tag{16}$$

where ρ_a is the material density; c is the specific heat capacity; V_a and S_a denote the volume and the surface area of the antenna panel, respectively; Q_p is the internal heat source density; k_x, k_y and k_z are the conductivity coefficients along the *x, y* and *z* directions, respectively; q^u and q^l are the heat fluxes of the upper and lower surfaces, respectively; and h_T is the convective exchange coefficient.

Using the finite element method, the temperature at an arbitrary point under three-dimensional heat conduction can be expressed as:

$$T(x, y, z, t) = \mathbf{N}(x, y, z)\, \mathbf{q}_T^e(t), \tag{17}$$

where $\mathbf{N}$ is the shape function matrix of the temperature field [62], and q_T^e represents the local nodal temperatures of the element. By substituting Eq. (17) into Eq. (16), the governing equation of the transient heat conduction is further recast as:

$$(\delta \mathbf{q}_T^e)^{\mathrm{T}} \left(\mathbf{M}_T^e \dot{\mathbf{q}}_T^e + \mathbf{K}_T^e \mathbf{q}_T^e - \mathbf{Q}_T^e\right) = 0\,, \tag{18}$$

where the element matrices can be derived as:

$$\begin{cases} \mathbf{M}_T^e = \displaystyle\int_{V_a} \rho c \mathbf{N}^{\mathrm{T}} \mathbf{N} dV_a \\ \mathbf{K}_T^e = \displaystyle\int_{S_2} h_T \mathbf{N}^{\mathrm{T}} \mathbf{N} dS_2 + \int_{V_a} \left[k_x \left(\frac{\partial \mathbf{N}}{\partial x}\right)^{\mathrm{T}} \left(\frac{\partial \mathbf{N}}{\partial x}\right) + k_y \left(\frac{\partial \mathbf{N}}{\partial y}\right)^{\mathrm{T}} \left(\frac{\partial \mathbf{N}}{\partial y}\right) + k_z \left(\frac{\partial \mathbf{N}}{\partial z}\right)^{\mathrm{T}} \left(\frac{\partial \mathbf{N}}{\partial z}\right)\right] dV_a \\ \mathbf{Q}_T^e = \displaystyle\int_{V_a} \mathbf{N}^{\mathrm{T}} Q_p dV_a + \int_{S_a} \mathbf{N}^{\mathrm{T}} q^u dS_a + \int_{S_a} \mathbf{N}^{\mathrm{T}} q^l dS_a + \int_{S_a} T_c h_T \mathbf{N}^{\mathrm{T}} \mathbf{q}_T^e dS_a \end{cases}. \tag{19}$$

It is worth noting that the temperature vector q_T^e is affected by the elastic deformation as well as the satellite motion, and the interaction prevents solving the time-dependent q_T^e directly from the heat conduction equations.

Moreover, the local temperature vector of the ith element q_T^e can be extracted from the global temperature vector of the system $\mathbf{q}_T$ by the Boolean matrix $\mathbf{B}_i$:

$$\mathbf{q}_T^e = \mathbf{B}_i \mathbf{q}_T. \tag{20}$$

On this basis, the governing equation of the heat conduction for the system is determined as:

$$\mathbf{M}_T \dot{\mathbf{q}}_T + \mathbf{K}_T \mathbf{q}_T - \mathbf{Q}_T = \mathbf{0} \tag{21}$$

where the generalized matrices $\mathbf{M}_T$, $\mathbf{K}_T$ and $\mathbf{Q}_T$ take the forms as:

$$\mathbf{M}_T = \sum_{i=1}^{n} \mathbf{B}_i^{\mathrm{T}} \mathbf{M}_T^e \mathbf{B}_i, \quad \mathbf{K}_T = \sum_{i=1}^{n} \mathbf{B}_i^{\mathrm{T}} \mathbf{K}_T^e \mathbf{B}_i, \quad \mathbf{Q}_T = \sum_{i=1}^{n} \mathbf{B}_i^{\mathrm{T}} \mathbf{Q}_T^e \mathbf{B}_i. \tag{22}$$

The temperature constraints can be further taken into account by introducing the Lagrange multiplier vector $\boldsymbol{\lambda}_T$. Finally, the transient heat conduction model of the system is obtained as:

$$\begin{cases} \mathbf{M}_T \dot{\mathbf{q}}_T + \mathbf{K}_T \mathbf{q}_T - \mathbf{Q}_T + \boldsymbol{\Gamma}_T^{\mathrm{T}} \boldsymbol{\lambda}_T = \mathbf{0} \\ \boldsymbol{\Gamma}(\mathbf{q}_T, t) = \mathbf{0} \end{cases}, \tag{23}$$

where $\boldsymbol{\Gamma}_T$ is the Jacobian matrix of the temperature constraint equation $\boldsymbol{\Gamma}(\mathbf{q}_T, t) = \mathbf{0}$.

3. Thermoelastic formulation of the antenna panel in absolute nodal coordinates

After obtaining the governing equation of heat conduction, we will focus on the dynamic response of the flexible system with thermal deformation. In this section, the thermoelasticity of the antenna panel will be incorporated into the motion equations of the antenna panel. Furthermore, an enhanced mathematical model will be developed to improve the solving efficiency.

3.1. Dynamic response of the flexible system with thermal deformation

Considering the shortcomings of the conventional finite element method and floating reference frame [56], a thermoelastic model of the antenna panel is developed via an enhanced absolute nodal coordinate formulation in this section. Note that the thickness and transverse deformation of the antenna panel are small compared to its length and width. Thus, it is appropriate to utilize the thin plate theory to describe the deformation of the panel.

For the thin plate, as illustrated in Fig. 3, the displacement field of the element only depends on the coordinates x and y. Different from the classical finite element method, the gradients rather than rotation angles are adopted to discard the traditional assumption of infinitesimal rotation, and the plate element with 36 degrees of freedom is described as:

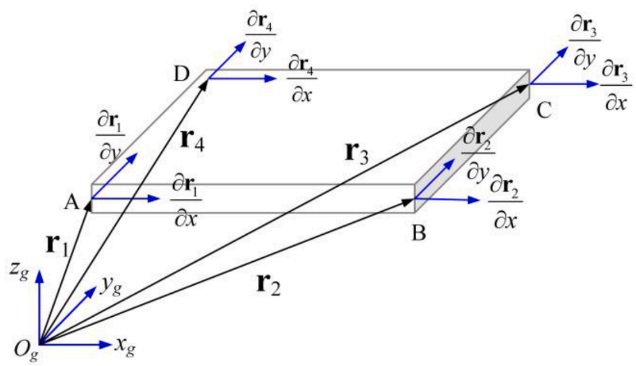

Fig. 3. *Four-node thin plate element with the absolute nodal coordinate formulation.* Gradients of absolute position vectors instead of rotations are adopted as nodal coordinates. The displacement field of the thin plate element is described by the reduced set that is only dependent on the spatial coordinates x and y.

$$\mathbf{e} = \left[\mathbf{r}_1^{\mathrm{T}}, \left(\frac{\partial \mathbf{r}_1}{\partial x}\right)^{\mathrm{T}}, \left(\frac{\partial \mathbf{r}_1}{\partial y}\right)^{\mathrm{T}}, \mathbf{r}_2^{\mathrm{T}}, \left(\frac{\partial \mathbf{r}_2}{\partial x}\right)^{\mathrm{T}}, \left(\frac{\partial \mathbf{r}_2}{\partial y}\right)^{\mathrm{T}}, \mathbf{r}_3^{\mathrm{T}}, \left(\frac{\partial \mathbf{r}_3}{\partial x}\right)^{\mathrm{T}}, \left(\frac{\partial \mathbf{r}_3}{\partial y}\right)^{\mathrm{T}}, \mathbf{r}_4^{\mathrm{T}}, \left(\frac{\partial \mathbf{r}_4}{\partial x}\right)^{\mathrm{T}}, \left(\frac{\partial \mathbf{r}_4}{\partial y}\right)^{\mathrm{T}} \right]^{\mathrm{T}}, \tag{24}$$

where $\mathbf{r}_1$, $\mathbf{r}_2$, $\mathbf{r}_3$ and $\mathbf{r}_4$ are the global position vectors of nodes A, B, C and D, respectively. In this formulation, an arbitrary point of the plate can be determined by:

$$\mathbf{r} = \mathbf{S}_{\mathrm{p}}(x, y, z)\mathbf{e}, \tag{25}$$

where $\mathbf{S}_{\mathrm{p}}$ is the shape function matrix as described in [63]. By using the virtual work principle, the mass matrix is derived as:

$$\mathbf{M}_P^e = \int_V \rho \mathbf{S}_{\mathrm{p}}^{\mathrm{T}} \mathbf{S}_{\mathrm{p}} dV, \tag{26}$$

where ρ is the density of the antenna panel. It can be seen from Eq. (26) that the mass matrix always remains constant since it only depends on the intrinsic properties and dimensions of the plate. As a result, both the centrifugal and Coriolis inertia forces are eliminated in the dynamic analysis.

Considering the thermal stress, the Green-Lagrange strain tensor $\boldsymbol{\varepsilon}$ is modified as [64]:

$$\boldsymbol{\varepsilon} = \left[\varepsilon_{xx}, \varepsilon_{yy}, 2\varepsilon_{xy}\right]^{\mathrm{T}} = \left[\frac{1}{2}\left(\frac{\partial \mathbf{r}}{\partial x}\right)^{\mathrm{T}}\left(\frac{\partial \mathbf{r}}{\partial x}\right) - \frac{1}{2} - \Delta T_1 \varpi_1, \quad \frac{1}{2}\left(\frac{\partial \mathbf{r}}{\partial y}\right)^{\mathrm{T}}\left(\frac{\partial \mathbf{r}}{\partial y}\right) - \frac{1}{2} - \Delta T_2 \varpi_2, \quad \left(\frac{\partial \mathbf{r}}{\partial x}\right)^{\mathrm{T}}\left(\frac{\partial \mathbf{r}}{\partial y}\right) \right]^{\mathrm{T}}, \tag{27}$$

where ϖ_1 and ϖ_2 are the thermal expansion coefficients along x and y directions, respectively, and ΔT_1 and ΔT_2 are the corresponding temperature differences. Besides, the curvature vector $\boldsymbol{\kappa}$ is formulated as:

$$\boldsymbol{\kappa} = \left[\kappa_{xx}, \kappa_{yy}, 2\kappa_{xy}\right]^{\mathrm{T}} = \left[\frac{\left(\frac{\partial^2 \mathbf{r}}{\partial x^2}\right)^{\mathrm{T}} \mathbf{n}}{\parallel \mathbf{n} \parallel^3}, \quad \frac{\left(\frac{\partial^2 \mathbf{r}}{\partial y^2}\right)^{\mathrm{T}} \mathbf{n}}{\parallel \mathbf{n} \parallel^3}, \quad 2\frac{\left(\frac{\partial^2 \mathbf{r}}{\partial x \partial y}\right)^{\mathrm{T}} \mathbf{n}}{\parallel \mathbf{n} \parallel^3}\right]^{\mathrm{T}}, \mathbf{n} = \frac{\partial \mathbf{r}}{\partial x} \times \frac{\partial \mathbf{r}}{\partial y}. \tag{28}$$

According to the Kirchhoff theory, the strain energy of the thin plate element under both axial and bending effects is

$$U = \frac{1}{2}\int_{V_f} \boldsymbol{\varepsilon}^{\mathrm{T}} \mathbf{E}_\varepsilon \boldsymbol{\varepsilon} dV_f + \frac{1}{2}\int_{V} \boldsymbol{\kappa}^{\mathrm{T}} \mathbf{E}_\kappa \boldsymbol{\kappa} dV_f. \tag{29}$$

For the isotropic homogenous material, the elastic coefficient matrices are defined as:

$$\mathbf{E}_\varepsilon = \frac{E_a}{1-\nu^2}\begin{bmatrix} 1 & \nu & 0 \\ \nu & 1 & 0 \\ 0 & 0 & (1-\nu)/2 \end{bmatrix}, \ \mathbf{E}_\kappa = \frac{h^3}{12}\mathbf{E}_\varepsilon, \tag{30}$$

where E_a is the Young's modulus, ν is the Poisson's ratio, and h is the thickness of the antenna panel.

The elastic force of the plate element Q_P^e is further derived as:

$$\mathbf{Q}_P^e = \left(\frac{\partial U}{\partial \mathbf{e}}\right)^{\mathrm{T}} = \mathbf{Q}_\varepsilon + \mathbf{Q}_K \tag{31}$$

with the components defined as below:

$$\begin{cases} \mathbf{Q}_\varepsilon = \int_{V_f} \frac{E_a}{1-\nu^2}\left(\varepsilon_{xx}\frac{\partial \varepsilon_{xx}}{\partial \mathbf{e}} + \varepsilon_{yy}\frac{\partial \varepsilon_{yy}}{\partial \mathbf{e}}\right) + \frac{2E_a}{1+\nu}\varepsilon_{xy}\frac{\partial \varepsilon_{xy}}{\partial \mathbf{e}} + \frac{\nu E_a}{1-\nu^2}\left(\varepsilon_{xx}\frac{\partial \varepsilon_{yy}}{\partial \mathbf{e}} + \varepsilon_{yy}\frac{\partial \varepsilon_{xx}}{\partial \mathbf{e}}\right) dV_f \\ \mathbf{Q}_\kappa = \int_{V_f} \frac{E_a h^3}{12(1-\nu^2)}\left(\kappa_{xx}\frac{\partial \kappa_{xx}}{\partial \mathbf{e}} + \kappa_{yy}\frac{\partial \kappa_{yy}}{\partial \mathbf{e}}\right) + \frac{E_a h^3}{6(1+\nu)}\kappa_{xy}\frac{\partial \kappa_{xy}}{\partial \mathbf{e}} + \frac{\nu E_a h^3}{12(1-\nu^2)}\left(\kappa_{xx}\frac{\partial \kappa_{yy}}{\partial \mathbf{e}} + \kappa_{yy}\frac{\partial \kappa_{xx}}{\partial \mathbf{e}}\right) dV_f \end{cases} \tag{32}$$

where V_f is the volume of the plate element.

According to Eq. (25), the following relationships stand:

$$\begin{cases} \frac{\partial \varepsilon_{xx}}{\partial \mathbf{e}} = \mathbf{S}_x^{\mathrm{T}} \mathbf{S}_x \mathbf{e} \\ \frac{\partial \varepsilon_{yy}}{\partial \mathbf{e}} = \mathbf{S}_y^{\mathrm{T}} \mathbf{S}_y \mathbf{e} \\ \frac{\partial \varepsilon_{xy}}{\partial \mathbf{e}} = \mathbf{S}_x^{\mathrm{T}} \mathbf{S}_y \mathbf{e} \end{cases}, \quad \begin{cases} \frac{\partial \kappa_{xx}}{\partial \mathbf{e}} = \frac{1}{\parallel \mathbf{n} \parallel^3}\left[\left(\frac{\partial^3 \mathbf{r}}{\partial x^2 \partial \mathbf{e}}\right)^{\mathrm{T}} \mathbf{n} + \left(\frac{\partial \mathbf{n}}{\partial \mathbf{e}}\right)^{\mathrm{T}} \frac{\partial^2 \mathbf{r}}{\partial x^2}\right] - \frac{3}{\parallel \mathbf{n} \parallel^5}\left(\frac{\partial^2 \mathbf{r}}{\partial x^2}\right)^{\mathrm{T}} \mathbf{n}\left(\frac{\partial \mathbf{n}}{\partial \mathbf{e}}\right)^{\mathrm{T}} \mathbf{n} \\ \frac{\partial \kappa_{yy}}{\partial \mathbf{e}} = \frac{1}{\parallel \mathbf{n} \parallel^3}\left[\left(\frac{\partial^3 \mathbf{r}}{\partial y^2 \partial \mathbf{e}}\right)^{\mathrm{T}} \mathbf{n} + \left(\frac{\partial \mathbf{n}}{\partial \mathbf{e}}\right)^{\mathrm{T}} \frac{\partial^2 \mathbf{r}}{\partial y^2}\right] - \frac{3}{\parallel \mathbf{n} \parallel^5}\left(\frac{\partial^2 \mathbf{r}}{\partial y^2}\right)^{\mathrm{T}} \mathbf{n}\left(\frac{\partial \mathbf{n}}{\partial \mathbf{e}}\right)^{\mathrm{T}} \mathbf{n} \\ \frac{\partial \kappa_{xy}}{\partial \mathbf{e}} = \frac{1}{\parallel \mathbf{n} \parallel^3}\left[\left(\frac{\partial^3 \mathbf{r}}{\partial x \partial y \partial \mathbf{e}}\right)^{\mathrm{T}} \mathbf{n} + \left(\frac{\partial \mathbf{n}}{\partial \mathbf{e}}\right)^{\mathrm{T}} \frac{\partial^2 \mathbf{r}}{\partial x \partial y}\right] - \frac{3}{\parallel \mathbf{n} \parallel^5}\left(\frac{\partial^2 \mathbf{r}}{\partial x \partial y}\right)^{\mathrm{T}} \mathbf{n}\left(\frac{\partial \mathbf{n}}{\partial \mathbf{e}}\right)^{\mathrm{T}} \mathbf{n} \end{cases}, \tag{33}$$

where the vectors $\mathbf{S}_x$ and $\mathbf{S}_y$ denote the partial derivatives of $\mathbf{S}_{\mathrm{p}}$ with respect to the coordinates x and y, respectively.

Using the standard assembling process [65], the motion equations of the antenna panel can be developed as:

$$\mathbf{M}\ddot{\mathbf{q}} + \mathbf{Q}_s(\mathbf{q}, \mathbf{q}_T) - \mathbf{Q}_f = \mathbf{0}. \tag{34}$$

In this equation, $\mathbf{q}$ is the global nodal coordinate vector of the system, and $\ddot{q}$ is the generalized acceleration vector. **M,** $\mathbf{Q}_s$, and $\mathbf{Q}_f$ are the generalized matrices of mass, elastic forces, and external forces, which are given by

$$\mathbf{M} = \sum_{i=1}^{n} \mathbf{T}_i^{\mathrm{T}} \mathbf{M}_P^e \mathbf{T}_i, \quad \mathbf{Q}_s = \sum_{i=1}^{n} \mathbf{T}_i^{\mathrm{T}} \mathbf{Q}_P^e \mathbf{T}_i, \quad \mathbf{Q}_f = \sum_{i=1}^{n} \mathbf{T}_i^{\mathrm{T}} \mathbf{Q}_w^e. \tag{35}$$

Here, $\mathbf{T}_i$ is the Boolean matrix of the displacement field that extracts Q_w^e is the external force that is imposed on the element.

In addition, considering the energy dissipation in the material due to internal friction, the damping force $\mathbf{Q}_d$ is expressed as:

$$\mathbf{Q}_d = \mathbf{D}_d \cdot \mathbf{q} = (\alpha_d \mathbf{M} + \beta_d \mathbf{K})\dot{\mathbf{q}}, \tag{36}$$

where $\mathbf{D}_d$ is the damping matrix. As formulated in previous research [56], the Rayleigh damping is adopted to evaluate $\mathbf{D}_d$ as a linear combination of mass and stiffness matrices with two damping coefficients α_d and β_d. According to the physical meaning of the stiffness matrix, **K** is calculated by:

$$\mathbf{Q}_d = \frac{\partial \mathbf{Q}_s(\mathbf{q}, \mathbf{q}_T)}{\partial \mathbf{q}}. \tag{37}$$

Mathematically, the constraint equations $\boldsymbol{\Phi}$ can be incorporated by introducing a Lagrange multiplier vector $\boldsymbol{\lambda}$. Finally, considering the thermal deformation, the dynamic response of the flexible system can be characterized in a compact form as below:

$$\begin{cases} \mathbf{M}\ddot{\mathbf{q}} + \boldsymbol{\Phi}_q^{\mathrm{T}} \boldsymbol{\lambda} + \mathbf{Q}_d + \mathbf{Q}_s(\mathbf{q}, \mathbf{q}_T) - \mathbf{Q}_f(\mathbf{q}, \cdot\mathbf{q}) = \mathbf{0} \\ \boldsymbol{\Phi}(\mathbf{q}, t) = \mathbf{0} \end{cases} \tag{38}$$

where $\boldsymbol{\Phi}_q$ is the Jacobi matrix of kinematic constraint equations.

3.2. Fast evaluation of elastic forces and their Jacobian matrices

It can be seen from Eq. (32) that high nonlinearities exist in the relationship between the elastic forces and nodal coordinates. Moreover, the motion equations of complex structures can only be solved by implicit algorithms, where the Jacobian matrix of the elastic force is indispensable. Since numerical differentiation is computationally inefficient and inaccurate, an enhanced solving strategy will be developed to calculate the elastic forces and the corresponding Jacobian matrices.

For the sake of description, we define:

$$\mathbf{D} = \mathbf{S}_x^{\mathrm{T}}\mathbf{S}_x, \mathbf{N} = \mathbf{S}_y^{\mathrm{T}}\mathbf{S}_y, \mathbf{H} = \mathbf{S}_x^{\mathrm{T}}\mathbf{S}_y. \tag{39}$$

Thereby, the following expressions can be obtained:

$$\frac{\partial \varepsilon_{xx}}{\partial \mathbf{e}_i} = \sum_{k=1}^{36} \mathbf{D}_{ki}\mathbf{e}_k, \quad \frac{\partial \varepsilon_{yy}}{\partial \mathbf{e}_i} = \sum_{k=1}^{36} \mathbf{N}_{ki}\mathbf{e}_k, \quad \frac{\partial \varepsilon_{xy}}{\partial \mathbf{e}_i} = \frac{1}{2}\left(\sum_{k=1}^{36} \mathbf{H}_{ki}\mathbf{e}_k + \sum_{m=1}^{36} \mathbf{H}_{im}\mathbf{e}_m\right). \tag{40}$$

Subsequently, by separating the variables with algebraic manipulations, the ith elastic force $(\mathbf{Q}_\varepsilon)_i$ induced by the tensile and shear deformations is derived as:

$$\begin{aligned}(\mathbf{Q}_\varepsilon)_i &= \int_{V_f} \frac{E_a}{1-\nu^2}\left(\varepsilon_{xx}\frac{\partial \varepsilon_{xx}}{\partial \mathbf{e}_i} + \varepsilon_{yy}\frac{\partial \varepsilon_{yy}}{\partial \mathbf{e}_i}\right) + \frac{2E_a}{1+\nu}\varepsilon_{xy}\frac{\partial \varepsilon_{xy}}{\partial \mathbf{e}_i} + \frac{\nu E_a}{1-\nu^2}\left(\varepsilon_{xx}\frac{\partial \varepsilon_{yy}}{\partial \mathbf{e}_i} + \varepsilon_{yy}\frac{\partial \varepsilon_{xx}}{\partial \mathbf{e}_i}\right) dV_f \\ &= \int_{V_f} \frac{E_a}{2(1-\nu^2)} \sum_{k=1}^{36}\sum_{m=1}^{36}\sum_{n=1}^{36} [(\mathbf{D}_{km}\mathbf{D}_{ni} + \mathbf{N}_{km}\mathbf{N}_{ni}) + \nu(\mathbf{D}_{km}\mathbf{N}_{ni} + \mathbf{N}_{km}\mathbf{D}_{ni})]\, dV_f (\mathbf{e}_k\mathbf{e}_m\mathbf{e}_n) + \\ &\quad \int_{V_f} \frac{E_a}{2(1+\nu)} \sum_{k=1}^{36}\sum_{m=1}^{36}\sum_{n=1}^{36} (\mathbf{H}_{km}\mathbf{H}_{ni} + \mathbf{H}_{km}\mathbf{H}_{in})\, dV_f (\mathbf{e}_k\mathbf{e}_m\mathbf{e}_n) - \\ &\quad \int_{V_f} \frac{E_a}{2(1-\nu^2)} \sum_{n=1}^{36} [(1+2\Delta T_1 \varpi_1)(\mathbf{D}_{ni} + v\mathbf{N}_{ni}) + (1+2\Delta T_2 \varpi_2)(\mathbf{N}_{ni} + v\mathbf{D}_{ni})]\, dV_f \mathbf{e}_n\end{aligned}, \tag{41}$$

where $\mathbf{e}_i$ denotes the ith term of the vector $\mathbf{e}$. In order to improve the computational efficiency, we especially introduce matrices $\mathbf{A}_1$, $\mathbf{A}_2$, $\mathbf{B}_1$ and $\mathbf{B}_2$ with the definitions as follows:

$$\begin{cases} (\mathbf{A}_1)_{kmni} = \displaystyle\int_{V_f} \frac{E_a}{2(1-\nu^2)}(\mathbf{D}_{km}\mathbf{D}_{ni} + \mathbf{N}_{km}\mathbf{N}_{ni}) + \nu(\mathbf{D}_{km}\mathbf{N}_{ni} + \mathbf{N}_{km}\mathbf{D}_{ni})dV_f \\ (\mathbf{A}_2)_{kmni} = \displaystyle\int_{V_f} \frac{E_a}{2(1+\nu)}(\mathbf{H}_{km}\mathbf{H}_{ni} + \mathbf{H}_{km}\mathbf{H}_{in})dV_f \\ (\mathbf{B}_1)_{ki} = \displaystyle\int_{V_f} \frac{E_a}{2(1-\nu^2)}(\mathbf{D}_{ki} + v\mathbf{N}_{ki})dV_f \\ (\mathbf{B}_2)_{ki} = \displaystyle\int_{V_f} \frac{E_a}{2(1-\nu^2)}(\mathbf{N}_{ki} + v\mathbf{D}_{ki})dV_f \end{cases}. \tag{42}$$

In detail, $(\mathbf{A}_j)_{kmni}$ $(j = 1,\ 2)$ is the term in the i-th row and the $(1296k + 36m + n - 1332)$-th column of $\mathbf{A}_j$, and $(\mathbf{B}_j)_{ki}$ $(j = 1,\ 2)$ denotes the term in the k-th row and the i-th column of $\mathbf{B}_j$. It is noticeable that $\mathbf{A}_1$, $\mathbf{A}_2$, $\mathbf{B}_1$ and $\mathbf{B}_2$ are constant matrices, which means that they can be reused after initialization. By taking advantage of these invariant matrices, the i-th elastic force $(\mathbf{Q}\varepsilon)_i$ is recast as

$$\begin{aligned}(\mathbf{Q}_\varepsilon)_i = &\sum_{k=1}^{36}\sum_{m=1}^{36}\sum_{n=1}^{36}\left((\mathbf{A}_1)_{kmni} + (\mathbf{A}_2)_{kmni}\right)\mathbf{e}_k\mathbf{e}_m\mathbf{e}_n - (1+2\Delta T_1\varpi_1)\sum_{k=1}^{36}(\mathbf{B}_1)_{ki}\mathbf{e}_k \\ &- (1+2\Delta T_2\varpi_2)\sum_{k=1}^{36}(\mathbf{B}_2)_{ki}\mathbf{e}_k.\end{aligned} \tag{43}$$

On this basis, the Jacobian matrix of the elastic force $(\mathbf{Q}_\varepsilon)_i$ is further evaluated as:

$$\begin{aligned}\frac{\partial(\mathbf{Q}_\varepsilon)_i}{\partial \mathbf{e}_j} = &\sum_{m=1}^{36}\sum_{n=1}^{36}\left[(\mathbf{A}_1)_{mnij} + 2(\mathbf{A}_1)_{mjni}\right]\mathbf{e}_m\mathbf{e}_n + \sum_{m=1}^{36}\sum_{n=1}^{36}\left[(\mathbf{A}_2)_{mnij} + (\mathbf{A}_2)_{mjni} + (\mathbf{A}_2)_{jmni}\right]\mathbf{e}_m\mathbf{e}_n - \\ &\left[(1+2\Delta T_1\varpi_1)(\mathbf{B}_1)_{ki} + (1+2\Delta T_2\varpi_2)(\mathbf{B}_2)_{ki}\right]\end{aligned}. \tag{44}$$

Similarly, the elastic force $\mathbf{Q}_\kappa$ that is induced by bending and torsion can also be derived, and the corresponding Jacobian matrix of $\mathbf{Q}_\kappa$ can be calculated accurately and efficiently like $\mathbf{Q}_\varepsilon$.

In this way, the invariant matrices that can be stored in advance are introduced to the derived analytical solutions, and the formulation of elastic forces is successfully separated from the variable nodal coordinates. That is, the developed method avoids calculating the integration over the volume of the element repeatedly and tediously. Consequently, the elastic forces and corresponding Jacobian matrices are solved precisely, and the computational efficiency is significantly improved.

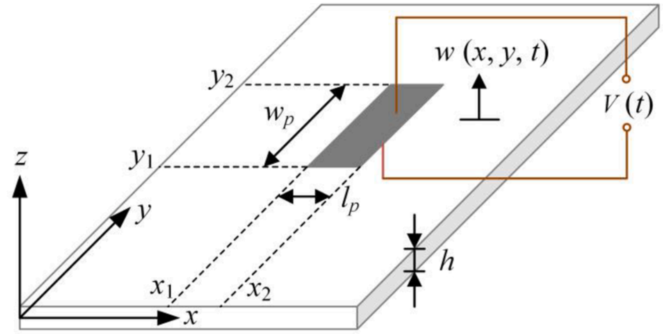

Fig. 4. *Piezoelectric transducer integrated on the antenna panel.* The piezoelectric patch is with the size of l_p (length) × w_p (width)× h_p (thickness), and its installation position can be determined by the coordinates of two opposite corners, namely (x_1, y_1) and (x_2, y_2). Excited by the thermally induced vibration *w* (*x*, *y*, *t*) of the panel, the piezoelectric transducer will generate electrical potential difference *V*(*t*).

4. Electromechanical analysis of the piezoelectric energy harvester

According to the comparison in the introduction, a piezoelectric transducer is preferred to be structurally integrated into the antenna panel for converting the thermally induced vibration into electricity. This section will develop a distributed-parameter electroelastic model of the piezoelectric transducer installed on the antenna panel to characterize the voltage output response. Moreover, the piezoelectric effect on the structural vibration will also be quantified.

4.1. Governing equation of the piezoelectric transducer

As shown in Fig. 4, a piezoelectric patch with the size of l_p (length) × w_p (width)× h_p (thickness) is boned on the antenna panel. The patch covers a rectangular area with two opposite corners at (x_1, y_1) and (x_2, y_2). Assuming that the size of the thin piezoelectric patch is much smaller than that of the antenna panel, its contributions to the global mass and stiffness matrices are thus negligible [66].

Since the piezoelectric material is generally transversely isotropic, its material properties in the constitutive equation satisfy:

$$c^p_{11} = c^p_{22}, \quad c^p_{12} = c^p_{21}, \quad e^p_{31} = e^p_{32}. \tag{45}$$

Here, $c^p_{11}c^p_{12}c^p_{22}c^p_{66}$ and c^p_{31} are the components of elastic stiffness, and *ep* 31 is the piezoelectric stress constant. In this study, the piezoelectric patch is polarized along the *z*-axis, and the electric field is given by:

$$E^e_1 = 0, \quad E^e_2 = 0, \quad E^e_3 = -V(t)\big/h_p, \tag{46}$$

where *V*(*t*) denotes the generated electrical potential difference, namely, the output voltage.

According to the material properties, the electroelastic constitutive equations of the piezoelectric transducer are expressed in a reduced form as:

$$\begin{bmatrix} F^p_1 \\ F^p_2 \\ F^p_6 \\ D^e_3 \end{bmatrix} = \begin{bmatrix} c^p_{11} & c^p_{12} & 0 & -e^p_{31} \\ c^p_{12} & c^p_{22} & 0 & -e^p_{31} \\ 0 & 0 & c^p_{66} & 0 \\ e^p_{31} & e^p_{31} & 0 & \varepsilon^p_{33} \end{bmatrix} \begin{bmatrix} S^p_1 \\ S^p_2 \\ S^p_6 \\ E^e_3 \end{bmatrix} = \begin{bmatrix} \mathbf{C}^e_p & -\mathbf{e}^e_p \\ \left(\mathbf{e}^e_p\right)^{\mathrm{T}} & \varepsilon^p_{33} \end{bmatrix} \begin{bmatrix} \mathbf{S}^e_p \\ E^e_3 \end{bmatrix}, \tag{47}$$

where F^p_1 and F^p_2denote the normal stress components in the directions of *x* and *y* axes, respectively; F^p_6 represents the shear stress in the *x*-*y* plane; S^p_1 and S^p_2 are the normal strain components along *x* and *y* axes, respectively; and S^p_6 is the shear strain component in the *x*-*y* plane. These strain components satisfy the following relationships:

$$S^p_1 = -h_{pc}\frac{\partial^2 w\,(x,y,t)}{\partial x^2}, \quad S^p_2 = -h_{pc}\frac{\partial^2 w\,(x,y,t)}{\partial y^2}, \quad S^p_6 = -h_{pc}\frac{\partial^2 w\,(x,y,t)}{\partial x \partial y}, \tag{48}$$

where h_{pc} is the distance from the center layer of the piezoelectric patch to the neutral surface of the antenna; *w* (*x*, *y*, *t*) is the transverse deflection of the panel at position (*x*, *y*) and time *t; D* ^{e} $_3$is the electric displacement in the direction of *z*-axis. Besides, ε^p_{33} is the equivalent permittivity constant. These components can be expressed as:

$$\begin{cases} c^p_{11} = \dfrac{s_{11}}{(s_{11}+s_{12})(s_{11}-s_{12})}, \quad c^p_{12} = \dfrac{-s_{12}}{(s_{11}+s_{12})(s_{11}-s_{12})} \\ c^p_{66} = \dfrac{1}{s_{66}}, \quad e^p_{31} = \dfrac{d_{31}}{s_{11}+s_{12}}, \quad \varepsilon^p_{33} = \varepsilon_{33} - \dfrac{2d^2_{31}}{s_{11}+s_{12}} \end{cases}, \tag{49}$$

where s_{11}, s_{12}, and s_{66} are the elastic compliance parameters, d_{31} is the piezoelectric constant, and ε_{33} is the permittivity component.

By adopting the Heaviside function *H* (·) to describe the areas with and without piezoelectric coverage, the internal moments of the piezoelectric patch are formulated as:

$$\begin{cases} M^p_1 = [H(x-x_1) - H(x-x_2)][H(y-y_1) - H(y-y_2)] \displaystyle\int F^p_1 z dz \\ M^p_2 = [H(x-x_1) - H(x-x_2)][H(y-y_1) - H(y-y_2)] \displaystyle\int F^p_2 z dz \\ M^p_6 = [H(x-x_1) - H(x-x_2)][H(y-y_1) - H(y-y_2)] \displaystyle\int F^p_6 z dz \end{cases}, \tag{50}$$

where the integrals are over the thickness of the piezoelectric patch. Under the thermal deformation, the internal bending moments of the antenna panel are determined by:

$$\begin{cases} M^s_1 = -\dfrac{Eh^3}{12(1-\nu^2)}\left(\dfrac{\partial^2 w\,(x,y,t)}{\partial x^2} + \nu\dfrac{\partial^2 w\,(x,y,t)}{\partial y^2}\right) \\ M^s_2 = -\dfrac{Eh^3}{12(1-\nu^2)}\left(\dfrac{\partial^2 w\,(x,y,t)}{\partial y^2} + \nu\dfrac{\partial^2 w\,(x,y,t)}{\partial x^2}\right) \\ M^s_6 = -\dfrac{Eh^3(1-\nu)}{12(1-\nu^2)}\dfrac{\partial^2 w\,(x,y,t)}{\partial x \partial y} \end{cases}. \tag{51}$$

Moreover, the partial differential equation of a thin plate with a small piezoelectric patch [66] is expressed as:

$$\frac{\partial^2\left(M^s_1 + M^p_1\right)}{\partial x^2} + \frac{\partial^2\left(M^s_2 + M^p_2\right)}{\partial y^2} + 2\frac{\partial^2\left(M^s_6 + M^p_6\right)}{\partial x \partial y} - \rho h\frac{\partial^2 w\,(x,y,t)}{\partial t^2} - c_p\frac{\partial w\,(x,y,t)}{\partial t} = 0. \tag{52}$$

Here, c_p is the viscous damping coefficient. By submitting Eqs. (47)–(51) into Eq. (52), the governing equation of the piezoelectric transducer is derived as:

$$\begin{aligned}&\frac{Eh^3}{12(1-\nu^2)}\left(\frac{\partial^4 w(x,y,t)}{\partial x^4}+\frac{\partial^4 w(x,y,t)}{\partial y^4}+2\frac{\partial^4 w(x,y,t)}{\partial x^2 y^2}\right)+\rho h\frac{\partial^2 w(x,y,t)}{\partial t^2}+c_p\frac{\partial w(x,y,t)}{\partial t}-\\&e^p_{31}h_{pc}V(t)[H(x-x_1)-H(x-x_2)]\left[\frac{d\delta(y-y_1)}{dy}-\frac{d\delta(y-y_2)}{dy}\right]-\\&e^p_{31}h_{pc}V(t)[H(y-y_1)-H(y-y_2)]\left[\frac{d\delta(x-x_1)}{dx}-\frac{d\delta(x-x_2)}{dx}\right]=0\end{aligned}\quad. \tag{53}$$

As formulated above, Eq. (53) describes the relationship between the electrical field and the mechanical field. The latter is determined by the motion equation of the piezoelectric energy system. In addition, the electrical circuit equation is further constructed to quantify the electrical current generated by the piezoelectric patch in response to the applied mechanical strain.

According to Gauss' flux theorem, the current flowing through the resistive load R_L is:

$$\frac{V(t)}{R_L}=\frac{\mathrm{d}}{\mathrm{d}t}\int_{y=y_1}^{y_2}\int_{x=x_1}^{x_2}\mathbf{D}^e\cdot\mathbf{n}^e\,\mathrm{d}x\mathrm{d}y=\frac{\mathrm{d}}{\mathrm{d}t}\int_{y=y_1}^{y_2}\int_{x=x_1}^{x_2}D^e_3\,\mathrm{d}x\mathrm{d}y, \tag{54}$$

where $\mathbf{D}^e$ is the electric displacement vector, and $\mathbf{n}^e$ is the unit vector outward from the electrode surface. Note that the only contribution to the inner product in Eq. (54) is from D^e_3. According to the electroelastic constitutive equations shown in Eq. (47), D^e_3 is equal to

$$D^e_3=e^p_{31}S^p_1+e^p_{31}S^p_2+\varepsilon^p_{33}E^e_3. \tag{55}$$

Substituting Eqs. (48) and (55) into Eq. (54) yields:

$$\frac{\mathrm{d}}{\mathrm{d}t}\int_{y=y_1}^{y_2}\int_{x=x_1}^{x_2}\left[-e^p_{31}h_{pc}\left(\frac{\partial^2 w(x,y,t)}{\partial x^2}+\frac{\partial^2 w(x,y,t)}{\partial y^2}\right)-\varepsilon^p_{33}\frac{V(t)}{h_p}\right]\mathrm{d}x\mathrm{d}y=\frac{V(t)}{R_L}. \tag{56}$$

For brevity, the capacitance of the piezoelectric patch C_p is defined as:

$$C_p=\left(l_p w_p\varepsilon^p_{33}\right)/h_p. \tag{57}$$

On this basis, Eq. (56) can be rewritten as:

$$C_p\frac{\mathrm{d}V(t)}{\mathrm{d}t}+\frac{V(t)}{R_L}+e^p_{31}h_{pc}\int_{y=y_1}^{y_2}\int_{x=x_1}^{x_2}\left(\frac{\partial^3 w(x,y,t)}{\partial x^2\partial t}+\frac{\partial^3 w(x,y,t)}{\partial y^2\partial t}\right)\mathrm{d}x\mathrm{d}y=0. \tag{58}$$

It is worth noting that the panel curvature can also be described in absolute nodal coordinates. According to the Kirchhoff plate theory, the mapping relationship is derived as below:

$$\begin{cases}\dfrac{\partial^2 w(x,y,t)}{\partial x^2}=-\dfrac{1}{z}\left(\dfrac{\partial\mathbf{r}}{\partial x}\right)^{\mathrm{T}}[1\ \ 0\ \ 0]^{\mathrm{T}},\ \dfrac{\partial^2 w(x,y,t)}{\partial y^2}=-\dfrac{1}{z}\left(\dfrac{\partial\mathbf{r}}{\partial y}\right)^{\mathrm{T}}[0\ \ 1\ \ 0]^{\mathrm{T}}\\ \dfrac{\partial^2 w(x,y,t)}{\partial x\partial y}=-\dfrac{1}{2z}\left(\dfrac{\partial\mathbf{r}}{\partial y}\right)^{\mathrm{T}}[1\ \ 0\ \ 0]^{\mathrm{T}}+\left(\dfrac{\partial\mathbf{r}}{\partial x}\right)^{\mathrm{T}}[0\ \ 1\ \ 0]^{\mathrm{T}}\end{cases}. \tag{59}$$

The above mapping relationship indicates that the third term on the left-hand side of Eq. (53) is a function of $\mathbf{q}$, d$\mathbf{q}$/dt, and $\mathbf{q}_T$. We have:

$$Q_v(\mathbf{q},\cdot\mathbf{q},\mathbf{q}_T)=e^p_{31}h_{pc}\int_{y=y_1}^{y_2}\int_{x=x_1}^{x_2}\left(\frac{\partial^3 w(x,y,t)}{\partial x^2\partial t}+\frac{\partial^3 w(x,y,t)}{\partial y^2\partial t}\right)\mathrm{d}x\mathrm{d}y. \tag{60}$$

Consequently, the governing equation of the piezoelectric transducer can be rewritten in the concise form as:

$$C_p\dot{V}+V/R_L+Q_v(\mathbf{q},\cdot\mathbf{q},\mathbf{q}_T)=0. \tag{61}$$

4.2. Electromechanically coupled model for the piezoelectric energy harvester plate

After obtaining the governing equation of the piezoelectric transducer, we will further quantify the piezoelectric effect on the structural vibration in this section. For the coupled electromechanical system, the generalized form of Hamilton's principle is expressed as:

$$\begin{aligned}&\int_{t=t_1}^{t_2}\left[\int\rho_a\delta\cdot\mathbf{u}^{\mathrm{T}}\cdot\mathbf{u}dV_a+\int\rho_p\delta\cdot\mathbf{u}^{\mathrm{T}}\cdot\mathbf{u}dV_p-\int\delta\mathbf{S}^{\mathrm{T}}_a\mathbf{C}_a\mathbf{S}_a dV_a-\int\delta\left(\mathbf{S}^e_p\right)^{\mathrm{T}}\mathbf{C}^e_p\mathbf{S}^e_p dV_p\right]dt+\\&\int_{t=t_1}^{t_2}\left[\int\delta\left(\mathbf{S}^e_p\right)^{\mathrm{T}}\mathbf{e}^e_p E^e_3 dV_p+\int\delta E^e_3\left(\mathbf{S}^e_p\right)^{\mathrm{T}}\mathbf{e}^e_p dV_p+\int\delta E^e_3\varepsilon^p_{33}E^e_3 dV_p\right]dt+\\&\int_{t=t_1}^{t_2}\left[\sum_{i=1}^{nf}\delta\mathbf{u}^{\mathrm{T}}(x_i,y_i,t)\mathbf{f}(x_i,y_i,t)+\sum_{i=1}^{nq}\delta V q(x_i,y_i,t)\right]dt=0\end{aligned} \tag{62}$$

where $\mathbf{u}$ is the vector of mechanical displacements along the three axes, $\mathbf{S}_a$ is the strain vector, $\mathbf{C}_a$ is the elastic stiffness matrix of the antenna panel, V_p is the volume of the piezoelectric patch, and V is the electrical potential difference. C^e_p, **S***e p* and **e***e p* are defined as Eq. (47). Besides, **f** (x_i, y_i, t) is the ith discrete mechanical force applied at the position (x_i, y_i), and q (x_i, y_i, t) is the ith electric charge output at the position (x_i, y_i). The total number of the forces and charges is n_f and n_q, respectively.

According to the constitutive relations of both the antenna panel and the piezoelectric patch, the strain-displacement and field-potential relations can be expressed as:

$$\mathbf{S}_a=\mathbf{L}_u\mathbf{u},\quad E^e_3=L_v V=\left(-1/h_p\right)V, \tag{63}$$

where the linear differential operator $\mathbf{L}_u$ is defined as [67]:

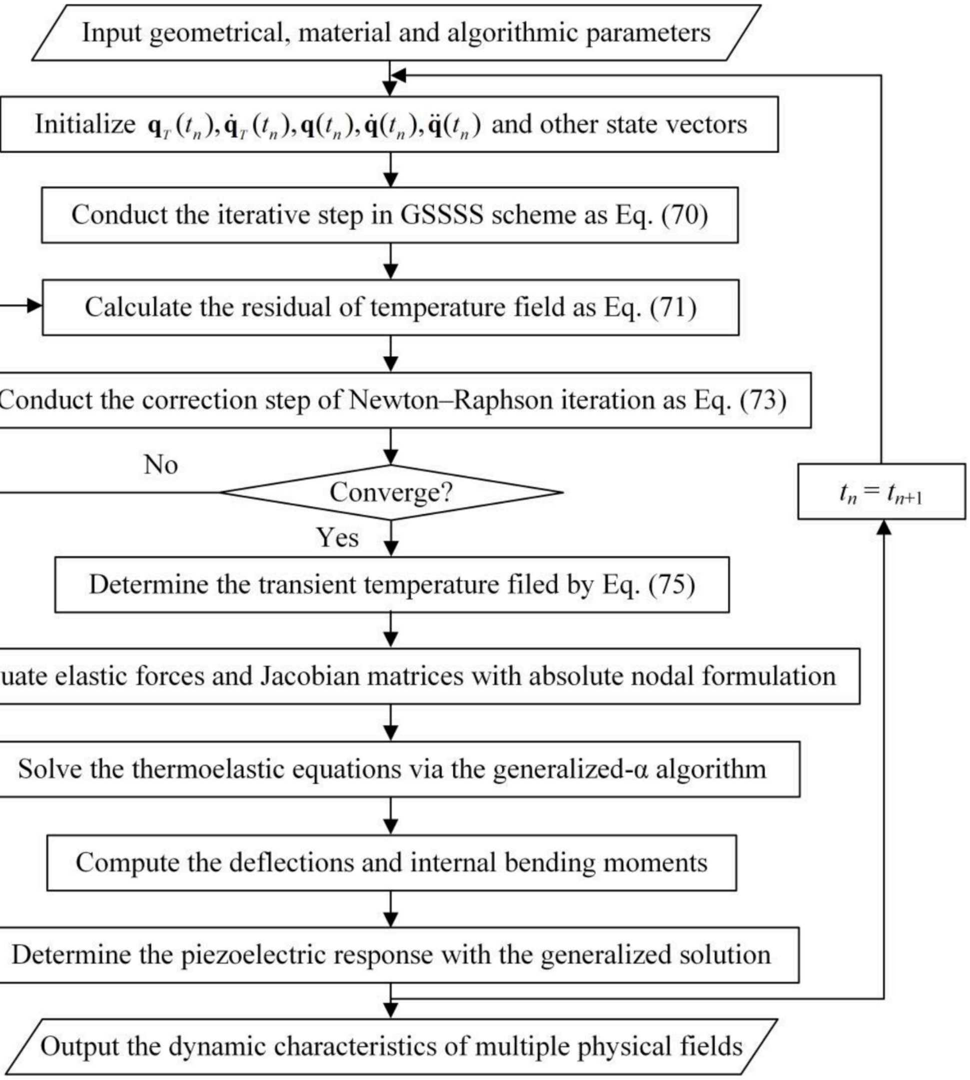

Fig. 5. *Procedures for implementing the proposed computational framework*. The GSSSS time integration scheme, the Newton–Raphson iteration, and the generalized-α algorithm are systematically integrated to solve the complicated multi-physics problem with second-order accuracy. The bidirectional thermoelastic interaction can be fully taken into account in this developed computational framework.

$$\mathbf{L}_u = \begin{bmatrix} \frac{\partial}{\partial x} & 0 & 0 \\ 0 & \frac{\partial}{\partial y} & 0 \\ \frac{\partial}{\partial y} & \frac{\partial}{\partial x} & 0 \end{bmatrix}. \tag{64}$$

Moreover, based on Eqs. (25) and (35), the displacement vector $\mathbf{u}$ can be extracted from the generalized coordinates $\mathbf{q}$ by:

$$\mathbf{u} = \mathbf{S}_\mathrm{p}(\mathbf{e} - \mathbf{e}_0) = \mathbf{S}_\mathrm{p}(\mathbf{T}_i\mathbf{q} - \mathbf{T}_i\mathbf{q}_0), \tag{65}$$

where $\mathbf{e}_0$ and $\mathbf{q}_0$ are the local and global absolute coordinates in the initial configuration.

After submitting Eqs. (63)–(65) into Eq. (62), we further utilize the variational principle to obtain the electromechanical coupling term $\Xi V(t)$, and the detailed derivation can be found in [68]. Specifically, the electromechanical coupling matrix Ξ is expressed as:

$$\varXi = \int \left[\left(\mathbf{L}_u \mathbf{S}_\mathrm{p} \mathbf{T}_i\right)^\mathrm{T} \left(\mathbf{e}_p^e\right)^\mathrm{T} \Big/ h_p \right] dV_p. \tag{66}$$

Finally, considering the piezoelectric effect on the structural vibration, the global equations of motion expressed in Eq. (38) are modified as:

$$\begin{cases} \mathbf{M}\ddot{\mathbf{q}} + \mathbf{\Phi}_q^\mathrm{T}\boldsymbol{\lambda} + \mathbf{Q}_d + \mathbf{Q}_s(\mathbf{q}, \mathbf{q}_T) + \varXi V - \mathbf{Q}_f(\mathbf{q}, \cdot\mathbf{q}) = \mathbf{0} \\ \mathbf{\Phi}(\mathbf{q}, t) = \mathbf{0} \end{cases}. \tag{67}$$

5. Integrated framework of the multi-physics problem

As aforementioned, the proposed system is expected to harvest energy from the antenna panel deformation induced by the time-varying thermal load. Since the whole energy harvesting process involves thermal-elastic and electromechanical couplings, an integrated framework of the multi-physics problem is unified in this section.

By taking account of all the couplings established in previous sections, the governing equations of the system are formulated as:

$$\begin{bmatrix} \mathbf{M}_T\mathbf{q}_T + \boldsymbol{\Gamma}_T^{\mathrm{T}}\boldsymbol{\lambda}_T + \mathbf{K}_T\mathbf{q}_T - \mathbf{Q}_T(\mathbf{q}, \mathbf{q}_T) \\ \mathbf{M}\ddot{\mathbf{q}} + \boldsymbol{\Phi}_q^{\mathrm{T}}\boldsymbol{\lambda} + \mathbf{Q}_d + \mathbf{Q}_s(\mathbf{q}, \mathbf{q}_T) + \boldsymbol{\Xi}V - \mathbf{Q}_f(\mathbf{q}, \cdot\mathbf{q}) \\ C_p\dot{V} + V/R_L + Q_v(\mathbf{q}, \cdot\mathbf{q}, \mathbf{q}_T) \\ \boldsymbol{\Gamma}\,(\boldsymbol{q}_T, t) \\ \boldsymbol{\Phi}(\mathbf{q}, t) \end{bmatrix} = \begin{bmatrix} \mathbf{0} \\ \mathbf{0} \\ 0 \\ \mathbf{0} \\ \mathbf{0} \end{bmatrix}. \tag{68}$$

To solve this complicated multi-physics problem, the mechanical displacement field and the transient temperature distribution should be first solved interactively and synchronously. Then, the displacement field is fed into the electromechanical equation to predict the voltage output from the piezoelectric transducer. In order to efficiently implement this solving strategy and improve the accuracy, an integrated computational framework is developed in this section.

Starting from the heat conduction analysis, the unified GSSSS time integration algorithm [69] is extended to solve the transient temperature in the space and time fields. To be more specific, the heat conduction equation given by Eq. (23) is firstly represented in the following form of incremental temperature:

$$\begin{cases} \mathbf{M}_T\widehat{\mathbf{q}}_T(t_n) + \mathbf{K}_T\bar{\mathbf{q}}_T(t_n) + \boldsymbol{\Gamma}_T^{\mathrm{T}}\bar{\boldsymbol{\lambda}}_T(t_n) = \bar{\mathbf{Q}}_T(t_n) \\ \boldsymbol{\Gamma}\,(\mathbf{q}_T, t_{n+1}) = \mathbf{0} \end{cases}. \tag{69}$$

In this equation, the introduced variables are determined as:

$$\begin{cases} \widehat{\mathbf{q}}_T(t_n) = \cdot\mathbf{q}_T(t_n) + \vartheta_1\Lambda_6\Delta\cdot\mathbf{q}_T \\ \bar{\mathbf{q}}_T(t_n) = \mathbf{q}_T(t_n) + \vartheta_1\Lambda_4\Delta t\cdot\mathbf{q}_T(t_n) + \vartheta_2\Lambda_5\Delta t\Delta\cdot\mathbf{q}_T \\ \bar{\boldsymbol{\lambda}}_T(t_n) = (1-\vartheta_1)\boldsymbol{\lambda}_T(t_n) + \vartheta_1\boldsymbol{\lambda}_T(t_{n+1}) \\ \bar{\mathbf{Q}}_T(t_n) = (1-\vartheta_1)\mathbf{Q}_T(t_n) + \vartheta_1\mathbf{Q}_T(t_{n+1}) \end{cases}, \tag{70}$$

where ϑ_i, Λ_i, and Θ_i ($i = 1, 2,\ldots, 6$) are the scaled parameters of the GSSSS algorithm [70]. However, different from the typical procedure of GSSSS method,$\Delta\dot{\mathbf{q}}_T$ cannot be directly obtained by solving Eq. (69) because $\mathbf{Q}_T$ depends on the temperature. To tackle the problem, the Newton–Raphson iteration is integrated into the GSSSS scheme to seek an accurate numerical solution in a more efficient manner.

If the following residual is still unsatisfactory after the iteration

$$\begin{bmatrix} \mathbf{R}_g \\ \mathbf{R}_c \end{bmatrix} = \begin{bmatrix} \mathbf{M}_T\widehat{\mathbf{q}}_T(t_n) + \mathbf{K}_T\bar{\mathbf{q}}_T(t_n) + \boldsymbol{\Gamma}_T^{\mathrm{T}}\bar{\boldsymbol{\lambda}}_T(t_n) - \mathbf{Q}_T(t_n) \\ \boldsymbol{\Gamma}\,(\mathbf{q}_T, t_n) \end{bmatrix}, \tag{71}$$

the below correction step is implemented to decrease the residual:

$$\Delta\mathbf{r} = \begin{bmatrix} \Delta\cdot\mathbf{q}_T \\ \Delta\boldsymbol{\lambda}_T \end{bmatrix} = -\begin{bmatrix} \partial\left(\mathbf{M}_T\widehat{\mathbf{q}}_T(t_n) + \mathbf{K}_T\bar{\mathbf{q}}_T(t_n) + \boldsymbol{\Gamma}_T^{\mathrm{T}}\bar{\boldsymbol{\lambda}}_T(t_n) - Q_T(t_n)\right)/\partial\cdot\mathbf{q}_T & \boldsymbol{\Gamma}_T^{\mathrm{T}} \\ \partial\boldsymbol{\Gamma}_T/\partial\cdot\mathbf{q}_T & \mathbf{0} \end{bmatrix}^{-1} \begin{bmatrix} \mathbf{R}_g \\ \mathbf{R}_c \end{bmatrix}. \tag{72}$$

Then, the state vector for the next numerical iteration step is modified as:

$$\begin{cases} \cdot\mathbf{q}_T(t_n) = \cdot\mathbf{q}_T(t_n) + \vartheta_1\Lambda_6\Delta\cdot\mathbf{q}_T \\ \mathbf{q}_T(t_n) = \mathbf{q}_T(t_n) + \vartheta_2\Lambda_5\Delta t\Delta\cdot\mathbf{q}_T \,. \\ \boldsymbol{\lambda}_T(t_n) = \boldsymbol{\lambda}_T(t_n) + \Delta\boldsymbol{\lambda}_T \end{cases} \tag{73}$$

If the difference of the norm of two consecutive correction vectors is smaller than the prescribed tolerance, namely,

$$\|\,\Delta\mathbf{r}_{k+1} - \Delta\mathbf{r}_k\|_2 < 10^{-8}, \tag{74}$$

the Newton-Raphson iteration converges, and the unknown vectors at the next time step are determined as:

$$\begin{cases} \cdot\mathbf{q}_T(t_{n+1}) = \cdot\mathbf{q}_T(t_n) + \Delta\cdot\mathbf{q}_T \\ \mathbf{q}_T(t_{n+1}) = \mathbf{q}_T(t_n) + \zeta_4\Delta t\cdot\mathbf{q}_T(t_n) + \zeta_5\Delta t\Delta\cdot\mathbf{q}_T \,. \\ \boldsymbol{\lambda}_T(t_{n+1}) = \boldsymbol{\lambda}_T(t_n) + \Delta\boldsymbol{\lambda}_T \end{cases} \tag{75}$$

After the transient temperature field is solved, the generalized-α algorithm [71] is further adopted to obtain the vibration response of the constrained mechanical system. In analogy with the iteration matrix shown as Eq. (71) in the Newton–Raphson method, the generalized-α algorithm also requires solving the nonlinear equations iteratively, and the Jacobian matrix of the elastic force in each time step has to be computed. As formulated in Eq. (43), the nodal coordinate vector and temperature difference have been taken out of the integral. By storing the invariant matrices in advance, the calculation of the elastic force is no longer a burdensome task. Moreover, the exact expression that is given in Eq. (44) enables the computation of the Jacobian matrix directly, reducing the computational cost in numerical differentiation. Once the generalized-α algorithm is converged, the vibration response of the panel can be updated, so can the transverse deflections and bending moments. Based on the determined $\mathbf{q}$,$\dot{\mathbf{q}}$ and $\mathbf{q}_T$, the voltage output of the piezoelectric transducer can be calculated from Eq. (61).

In this computational framework, the integrated GSSSS time integration scheme, the Newton–Raphson iteration and the generalized-α algorithm are of second-order accuracy [70,71]. In this process, the system variables are iteratively solved at a time step of 10^{-4} s. Fig. 5 presents the step-by-step procedures for implementing the proposed computational framework.

6. Case study

In this section, the proposed method will be utilized to predict the dynamic response of an antenna panel under time-varying thermal load, particularly the capability of the attached piezoelectric transducer to harness energy from thermally induced vibrations. Moreover, the results from the proposed method will be verified by comparing with the simulation results.

6.1. Numerical example

As depicted in Fig. 6, a thin piezoelectric patch is bonded on the surface of an antenna panel. Considering that the transmit/receive module cells are uniformly distributed in the middle of the panel, it is preferred to integrate the piezoelectric patch on the frame at the edge of the panel. This layout not only ensures the bonding reliability, but also avoids the interference with functional components. The geometric and material parameters of the antenna panel and piezoelectric patch are listed in Table 1 and Table 2, respectively. Besides, the satellite orbit height is 631 km. The angle between the antenna panel and the tangent plane of the Earth is 7.92°. To consistently describe the multi-physics, a global coordinate system O_g-$x_g y_g z_g$ is established with the original point O_g at the midpoint of the left surface of the panel, as illustrated in Fig. 6.

In reality, when the satellite moves from the twilight zone into the light zone, the temperature of the antennal panel changes dramatically, and the sudden heating on the panel can cause large deformation and

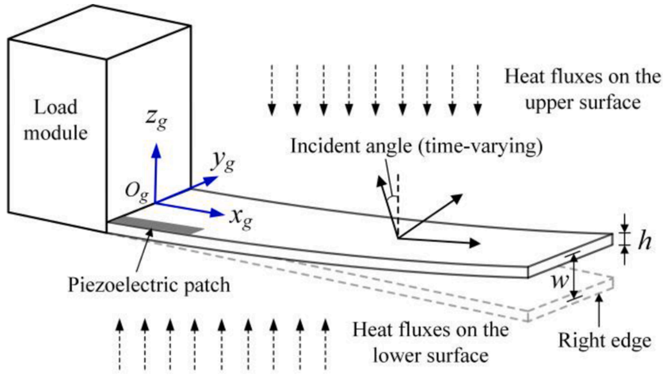

Fig. 6. *Schematic of antenna panel deformation under spatial heat fluxes*. The incident angles of heat fluxes are actually time-varying because of the deformation and vibration of the antenna panel. By attaching a piezoelectric patch onto the antenna panel, the kinetic energy from the thermally induced vibration is converted into electrical energy.

Table 1
Geometric and material parameters of the antenna panel.

Properties	Nomenclature	Values
Length	l	1.2 m
Width	w_s	0.8 m
Thickness	h	0.05 m
Mass density	ρ_a	1.75×10^3 kg/m^3
Elastic modulus	E_a	2.07×10^{11} Pa
Poisson's ratio	ν	0.3
Thermal expansion coefficients	ϖ_1 and ϖ_2	2.3×10^{-4} 1/K
Conductivity coefficients	k_x, k_y and k_z	1.5 W/(m K)
Specific heat capacity	c	952 J/(kg K)
Absorptivity of the solar radiation	α_m	0.79
Absorptivity of the Earth-emitted radiation	α_e	0.7
Emissivity of the surface	ς_p	0.7

Table 2
Geometric and material parameters of the piezoelectric patch.

Properties	Nomenclature	Values
Length	l_p	300 mm
Width	w_p	100 mm
Thickness	h_p	2 mm
Elastic compliance	s_{11}	16.50 pm^2/N
Elastic compliance	s_{12}	–4.78 pm^2/N
Elastic compliance	s_{66}	42.60 pm^2/N
Piezoelectric constant	d_{31}	–190 pm/V
Permittivity constant	ε_{33}	10.38 nF/m

thermal flutter. Therefore, this typical transition process is pretty suitable to implement energy harvesting. We will take it as an example to investigate the feasibility of the proposed scheme. The moment when the satellite is at the boundary between the shadow and twilight zones is set as t_0. Besides, the temperature of the panel is initialized as the ambient temperature, i.e., $T_0 = 273.15$ K.

7. Results and discussions

Given the orbit height, the satellite needs to rotate 0.58° to get out of the twilight zone. According to the law of universal gravitation, the time to complete the movement is calculated to be 8.64 s. During this transition process, the lower surface of the panel is an anode, while the upper surface is a cathode. The time-varying heat fluxes applied on the antenna panel are determined and shown in Fig. 7. It can be seen that the total heat flux on the lower surface dramatically increases from 129.13 to 1142.85 W/m^2, while that of the upper surface is nearly unchanged.

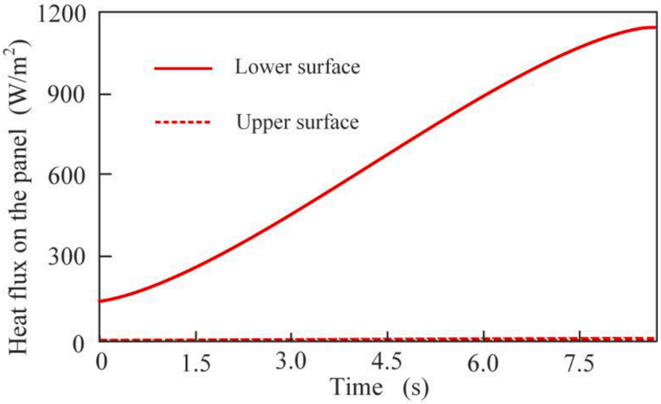

Fig. 7. *Spatial heat fluxes applied on the antenna panel*. When the satellite travels from the twilight zone into the light zone, the lower surface of the panel is an anode, while the upper surface is a cathode. The total heat fluxes applied on the upper and lower surfaces are of different densities. Sudden heating occurs on the lower surface of the panel.

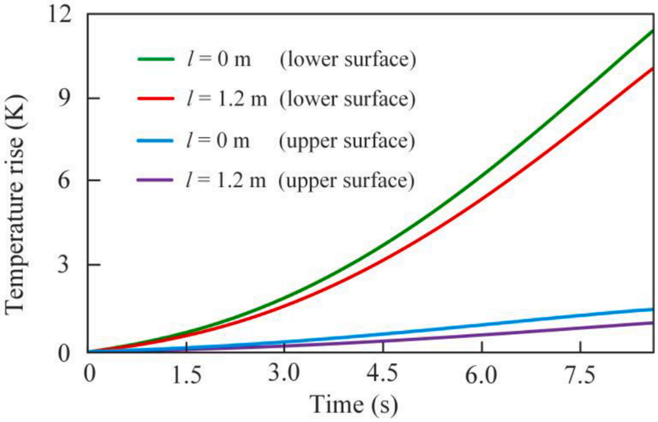

Fig. 8. *Temperature distribution of the antenna panel at different instants*. During the transition from the twilight zone into the light zone, the temperature rises at the left and right edges of the lower and upper surfaces are different.

The temperature field is discretized using the 3D 8-node hexahedral element. The interaction between heat conduction and structural deformation is fully considered. In order to guarantee the accuracy in the iterative calculation, the maximum integration step-size is set to 10^{-4} s, and the absolute tolerance is 10^{-8}. The calculated temperature distributions of the antenna panel at different instants are illustrated in Fig. 8. The temperature on the left edge of the panel rises at a higher rate than on the right edge. Moreover, significant temperature differences exist between the lower surface and upper surfaces.

To comprehensively reveal the thermal-elastic-electric coupling effect on the antenna panel, the results of both partially and fully coupled models are provided. In the partially coupled model, the absorbed heat flux is directly determined from the initial configuration. In other words, the bidirectionally coupled problem is simplified into a unidirectionally coupled one. As to the fully coupled method, after solving the thermally induced deformation in each time step, it is required that the absorbed thermal energy should be updated timely to evaluate the effect of structural deformation on the incident angle of heat flux. Particularly, it is pointed out that both partially and fully coupled models incorporate the interaction between the piezoelectric effect and the structural vibration. Based on the developed analytical model and computational framework, the dynamic response of the piezoelectric energy harvester is determined. Moreover, this multi-physics problem is also simulated using the software COMSOL (version 5.4). For these simulations, the Rayleigh damping coefficients α_d and β_d are set as 1.357×10^{-3} s^{-1} and

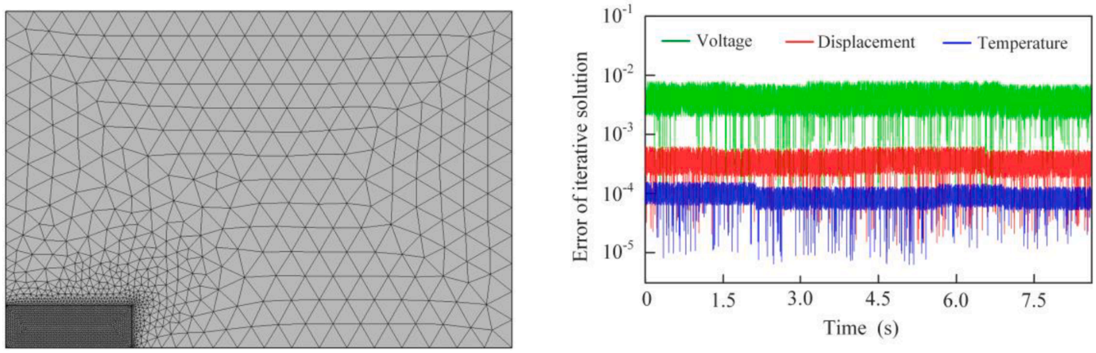

(a) COMSOL mesh model

(b) Relative error during the iterative calculation

Fig. 9. *Simulation in COMSOL*. The meshes are shaped by the physics control at the finer level to strike a balance between accuracy and efficiency. For the temperature, displacement and voltage, their maximum iteration errors between the numeric and exact solutions are smaller than 10^{-2}.

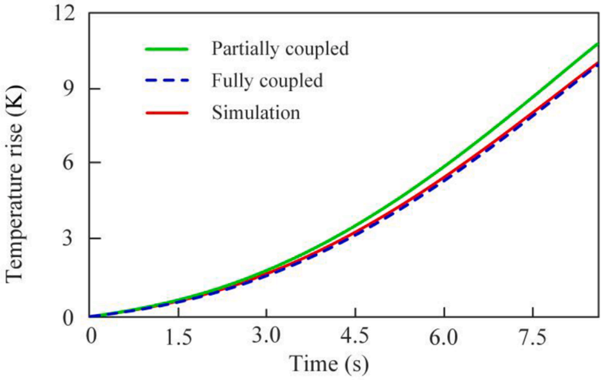

(a) Temperature change at the right edge of the lower surface of the antenna panel.

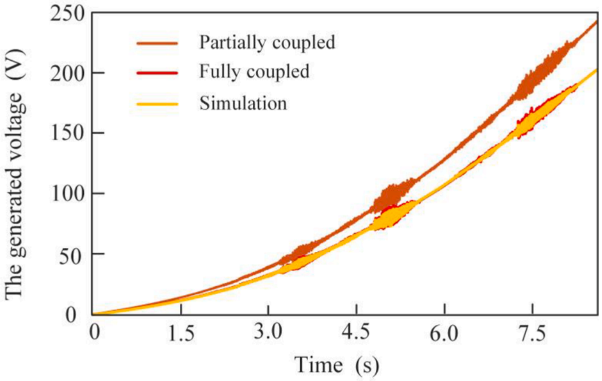

(c) Dynamic response of the piezoelectric energy harvester.

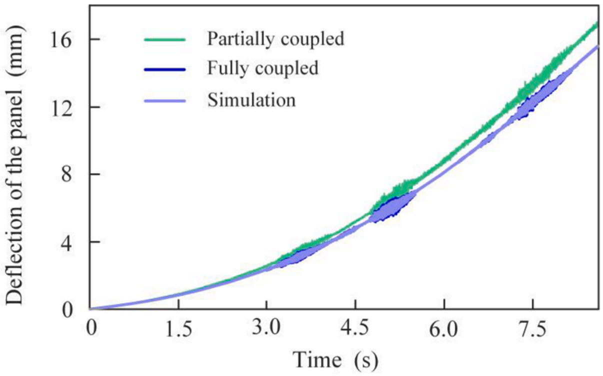

(b) Bending deformation of the antenna panel.

Fig. 10. *Comparison of the results obtained from the simulation, partially and fully coupled models*. The partially coupled model only considers the unidirectional coupling between heat absorption and structural deformation. The fully coupled model developed in this work takes the bidirectional thermoelastic interaction into account. Additionally, the bidirectional coupling between the piezoelectric effect and the structural vibration is incorporated into the three models.

5.289×10^{-5} s, respectively, which are the original and nominal values of the material. After a mesh convergence study, the PEH is discretized with finer meshes, as graphically depicted in Fig. 9(a). The iteration errors between the numerical and exact solutions are shown in Fig. 9(b), which indicates that the maximum error is smaller than 10^{-2}. Besides, the difference between the voltage outputs obtained by the finer and extra-fine mesh models is slight. Therefore, the result from the finer mesh model can be deemed as converged with satisfactory accuracy.

For the multi-physics coupled problem, Fig. 10(a) presents the temperature rise of the antenna panel at the right edge of the lower surface. Fig. 10(b) depicts the bending deformation at the midpoint of the right surface. Fig. 10(c) shows the voltage output responses from different methods. As seen in Fig. 10, the numerical predictions of the fully coupled model are in good agreement with the simulations. However, the deflections and voltages obtained by the partially coupled model are larger than those of the fully coupled model at the same instant, and their vibration amplitudes are also different. To explain this phenomenon, the normal unit vector of a finite element at the right top corner is illustrated, and its projection onto the z_g axis is given in Fig. 11. According to the physical definition, the projection reflects the cosine of the incident angle of the heat flux. It is observed that the projection tends to gradually decrease with unsmooth fluctuations, which means that the incident angle varies with the structural deformation. In other words, thermal deformation also has a backward effect on thermal absorption. For this reason, the partially coupled model that neglects the angular change cannot accurately reveal the thermal flutter effect, and

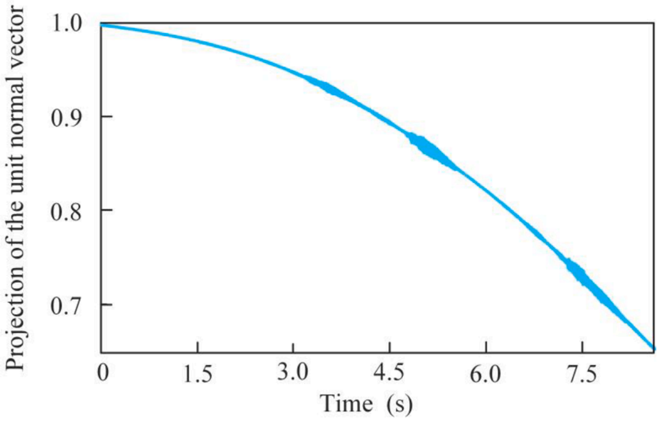

Fig. 11. *Time history of the projection of the normal unit vector*. The projection variation indicates that the incident angle of the heat flux is time-varying; thus, the structural deformation also has a backward effect on the heat absorption.

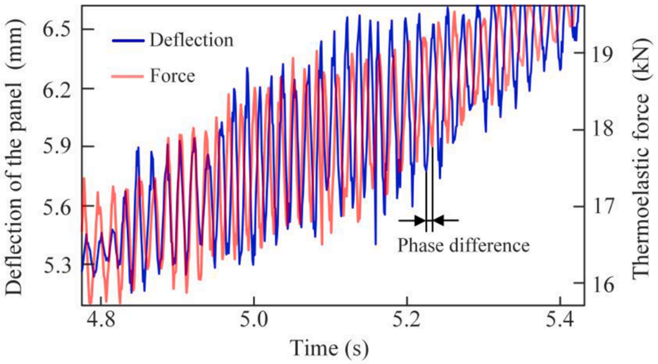

Fig. 12. *Phase difference between the thermoelastic forces and the structural displacements*. When the high frequency "beating" phenomenon occurs, the thermoelastic forces oscillate, and there exists a phase difference between the thermoelastic forces and the structural displacements.

this error further propagates into the results of the voltage.

As highlighted in Fig. 10(b), another interesting feature is the occurrence of the high-frequency "beating" phenomenon. It is found that the high-frequency thermal flutter is associated with two factors: (1) the oscillation of thermoelastic forces; (2) the phase difference between the thermoelastic forces and the structural displacements. As shown in Fig. 12, a phase difference exists between the dynamic responses of the thermoelastic force and the antenna panel deflection, triggering the thermoelastic force to do work on the antenna panel. If the sum of work done by thermoelastic and damping forces is positive, the amplitude of the thermally induced vibration will increase continuously, i.e., the high-frequency flutter occurs. In contrast, if the sum of work done by thermoelastic and damping forces is negative, the oscillation amplitude decays with time and the thermal flutter fades away.

The differences between the numerical predictions and simulation results are quantified in Fig. 13. The maximum relative errors of the deflection and generated voltage are smaller than 5.7%, indicating that the analytical solutions are of satisfactory accuracy. In addition, it takes 507,164.8 s to complete the numerical calculation of the transition process with MATLAB 2020b, while 647,266.3 s to complete the multi-physics simulation with COMSOL. It is obvious that the developed computation strategy has a higher efficiency in dealing with the thermal-mechanical-electrical coupling problem.

As discussed above, the proposed method can effectively and efficiently predict the dynamic response of the energy harvesting system. Moreover, the full consideration of the interaction between structural deformation and heat absorption yields a more accurate prediction of the voltage output response. During the transition from the twilight to the light zone, it is shown that the output voltage gradually increases with fluctuations. Given that the resistive load is of 1 kΩ, the efficiency of converting the thermal energy into electrical energy is presented in Fig. 14. In terms of the single piezoelectric patch, although the conversion efficiency of the system is lower than that of the solar batteries, two fascinating features of the designed system are worth being

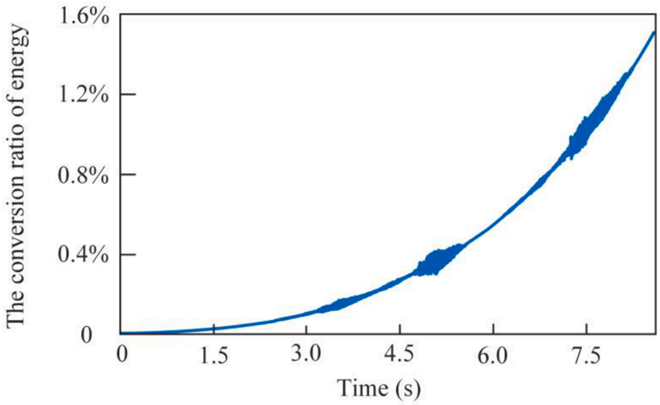

Fig. 14. *Conversion ratio of the thermal energy into electrical energy*. In terms of the single piezoelectric patch, the conversion efficiency of the system increases with the satellite movement from the twilight zone into the light zone, and the maximum conversion efficiency is less than 1.6%.

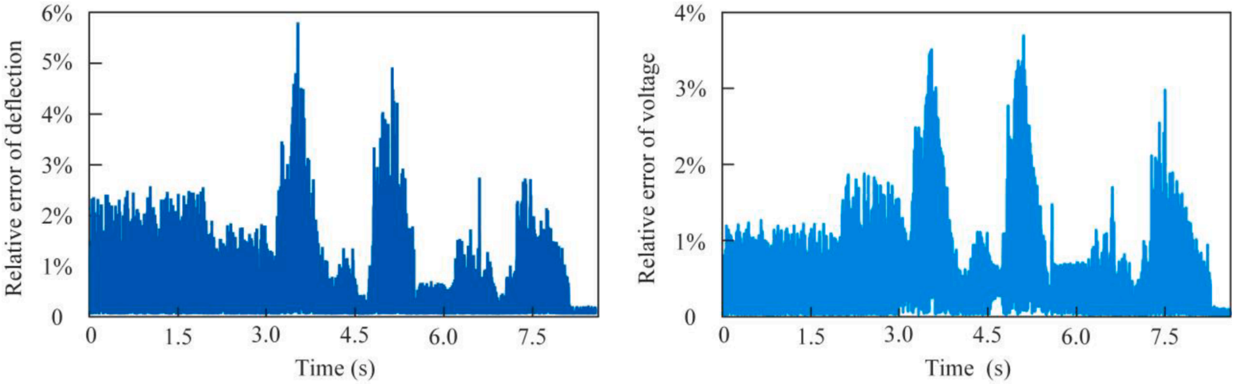

(a) Relative error of the deflection.

(b) Relative error of the output voltage.

Fig. 13. *Relative error between the numerical and simulation results*. The maximum relative error of the deflection and the output voltage is smaller than 6% and 4%, respectively, which indicates that the results obtained from the fully coupled model are of good accuracy.

highlighted. On the one hand, the maximum output voltage is up to 202.169 V, which is enough to drive sensors and actuators for shape adjustment. On the other hand, the electric energy applied to reduce the thermal deformation originates from thermally induced vibration, and this operation enables a new paradigm of physical intelligence. Note that since the upper and lower surfaces of the antenna panel periodically turn to the sunny side, the output power will not monotonically increase as the temperature difference diminishes. In fact, it can be observed in Fig. 10(b) that the amplitudes of the thermally induced vibration approach zero after the satellite enters the light zone. That is, the high-frequency beating phenomenon tends to disappear gradually. These results provide pivotal insights into the design considerations of piezoelectric systems for harnessing energy from thermally induced vibrations of antenna panels.

8. Conclusions

This paper has, for the first time, proposed integrating a piezoelectric transducer onto the antenna panel of a satellite in outer space to harvest energy from thermally induced vibrations. A novel analytical methodology and a computational framework have been developed to reveal the dynamic responses of the system under the complicated thermal-mechanical-electrical coupling effect. The accuracy and efficiency of the developed method have been verified through a comparison with the simulation results. Based on numerical results and technical discussions, some main conclusions are remarked as follows:

(1) The proposed fully coupled model can accurately and efficiently predict the transient response of the heat conduction, thermally induced vibration, and piezoelectric effect, providing comprehensive insights into the coupling characteristics of the multiphysics problem.
(2) The bidirectional interaction between the elastic deformation and the heat absorption plays a significant role in the thermally induced vibration of the antenna panel. It is inappropriate to assume that the temperature distribution is independent of the panel deflections.
(3) The deflection of the antenna panel under the time-varying thermal loading contains the quasi-static displacement and the superimposed vibration. If the phase difference exists between the oscillating thermoelastic forces and the structural displacements, the thermal flutter may occur.
(4) The maximum output voltage of the designed PEH is up to 202.169 V, which shows the potential of harvesting energy from the thermally induced vibration of antenna panels to produce a considerable power output for wireless electronic devices.

To summarize, this study not only innovatively extends the application of energy harvesting technology to the circumstances with thermally induced vibration phenomena, but also provides a comprehensive analytical and computational scheme for predicting the dynamic responses of thermal-mechanical-electrical coupled systems. Moreover, the investigation results offer useful insights into the design of PEH, which employs the thermally induced vibration as a potential power supply. Since the time-space scale of the problem is large and more practical constraints are required to be considered, the distribution and parameters of piezoelectric patches will be refined in further works.

CRediT authorship contribution statement

Dewen Yu: Methodology, Software, Validation, Writing – original draft. **Yaowen Yang:** Conceptualization, Supervision. **Guobiao Hu:** Investigation, Formal analysis, Writing – review & editing. **Yifan Zhou:** Software, Validation. **Jun Hong:** Supervision, Funding acquisition.

Declaration of Competing Interest

The authors declare that they have no known competing financial interests or personal relationships that could have appeared to influence the work reported in this paper.

Data availability

No data was used for the research described in the article.

Acknowledgments

The work is financed by National Natural Science Foundation of China (Grant No. 51635010). The authors also appreciate the valuable discussion with Feifei Chen, who is an engineer of the Institute of Aerospace Systems Engineering in Shanghai.

References

[1] Elahi H, Butt Z, Eugnei M, Gaudenzi P, Israr A. Effects of variable resistance on smart structures of cubic reconnaissance satellites in various thermal and frequency shocking conditions. J Mech Sci Technol 2017;31:4151–7.
[2] Nie R, He B, Yan S, Ma X. Design optimization of mesh antennas for on-orbit thermal effects. Int J Mech Sci 2020;175:105547.
[3] Kajiwara I, Kitabatake S, Hosoya N, Maeda S. Design of dielectric elastomer actuators for vibration control at high frequencies. Int J Mech Sci 2019;157:849–57.
[4] Lu G, Zhou J, Cai G, Fang G, Lv L, Peng F. Studies of thermal deformation and shape control of a space planar phased array antenna. Aerosp Sci Technol 2019;93:105311.
[5] Zhou J, Kang L, Tang B, Tang B, Huang J, Wang C. Adaptive compensation of flexible skin antenna with embedded fiber Bragg grating. IEEE Trans Antennas Propag 2019;67:4385–96.
[6] Hiruta T, Hosoya N, Maeda S, Kajiwara I. Experimental validation of vibration control in membrane structures using dielectric elastomer actuators in a vacuum environment. Int J Mech Sci 2021;191:106049.
[7] Daliri A, Galehdar A, John S, Wang CH, Rowe WS, Ghorbani K. Wireless strain measurement using circular microstrip patch antennas. Sens Actuators A 2012;184:86–92.
[8] Choi J, Hwang K, Kim B. Reliability analysis for thermal cutting method based non-explosive separation device. J Mech Sci Technol 2016;30:5433–8.
[9] Ma H, Yan B, Zhang L, Zheng W, Wang P, Wu C. On the design of nonlinear damping with electromagnetic shunt damping. Int J Mech Sci 2020;175:105513.
[10] Slongo L, Martínez S, Eiterer B, Pereira T, Bezerra E, Paiva K. Energy-driven scheduling algorithm for nanosatellite energy harvesting maximization. Acta Astronaut 2018;147:141–51.
[11] Tsushima N, Su W. A study on adaptive vibration control and energy conversion of highly flexible multifunctional wings. Aerosp Sci Technol 2018;79:297–309.
[12] Takacs A, Aubert H, Fredon S, Despoisse L, Blondeaux H. Microwave power harvesting for satellite health monitoring. IEEE Trans Microw Theory Tech 2014;62:1090–8.
[13] Carneiro P, Soares dos Santos MP, Rodrigues A, Ferreira JAF, Simões JAO, Marques AT, Kholkin AL. Electromagnetic energy harvesting using magnetic levitation architectures: a review. Appl Energy 2020;260:114191.
[14] Liang H, Hao G, Olszewski OZ, Pakrashi V. Ultra-low wide bandwidth vibrational energy harvesting using a statically balanced compliant mechanism. Int J Mech Sci 2022;219:107130.
[15] Pyo S, Kwon DS, Ko HJ, Eun Y, Kim J. Frequency up-conversion hybrid energy harvester combining piezoelectric and electromagnetic transduction mechanisms. Int J Precis Eng Manuf Green Technol 2022;9:241–51.
[16] Fan K, Cai M, Wang F, Tang L, Liang J, Wu Y, Qu H, Tan Q. A string-suspended and driven rotor for efficient ultra-low frequency mechanical energy harvesting. Energy Convers Manag 2019;198:111820.
[17] Li Z, Liu Y, Yin P, Peng Y, Luo J, Xie S, Pu H. Constituting abrupt magnetic flux density change for power density improvement in electromagnetic energy harvesting. Int J Mech Sci 2021;198:106363.
[18] Park K, Lee D, Seo J. Dual-polarized GPS antenna array algorithm to adaptively mitigate a large number of interference signals. Aerosp Sci Technol 2018;78:387–96.
[19] Dong L, Closson AB, Jin C, Trase I, Chen Z, Zhang JX. Vibration-energy-harvesting system: transduction mechanisms, frequency tuning techniques, and biomechanical applications. Adv Mater Technol 2019;4:1900177.
[20] Sun W, Jiang Z, Xu X, Han Q, Chu F. Harmonic balance analysis of output characteristics of free-standing mode triboelectric nanogenerators. Int J Mech Sci 2021;207:106668.
[21] He J, Qian S, Niu X, Zhang N, Qian J, Hou X, Mu J, Geng W, Chou X. Piezoelectric-enhanced triboelectric nanogenerator fabric for biomechanical energy harvesting. Nano Energy 2019;64:103933.
[22] Kim HS, Kim JH, Kim J. A review of piezoelectric energy harvesting based on vibration. Int J Precis Eng Manuf 2011;12:1129–41.

[23] Lu Z, Chen J, Ding H, Chen L. Two-span piezoelectric beam energy harvesting. Int J Mech Sci 2020;175:105532.

[24] Yang B, Yun KS. Piezoelectric shell structures as wearable energy harvesters for effective power generation at low-frequency movement. Sens Actuators A 2012;188:427–33.

[25] Moradi-Dastjerdi R, Behdinan K, Safaei B, Qin Z. Buckling behavior of porous CNT-reinforced plates integrated between active piezoelectric layers. Eng Struct 2020;222:111141.

[26] Li Z, Peng X, Hu G, Peng Y. Theoretical, numerical, and experimental studies of a frequency up-conversion piezoelectric energy harvester. Int J Mech Sci 2022;223:107299.

[27] Yang K, Zhang Z, Zhang Y, Huang H. High-resolution monitoring of aerospace structure using the bifurcation of a bistable nonlinear circuit with tunable potential-well depth. Aerosp Sci Technol 2019;87:98–109.

[28] Li Z, Peng X, Hu G, Zhang D, Xu Z, Peng Y. Towards real-time self-powered sensing with ample redundant charges by a piezostack-based frequency-converted generator from human motions. Energy Convers Manag 2022;258:115466.

[29] Wang G, Lu Y. An improved lumped parameter model for a piezoelectric energy harvester in transverse vibration. Shock Vib 2014;2014:935298.

[30] Dhote S, Yang Z, Behdinan K, Zu J. Enhanced broadband multi-mode compliant orthoplanar spring piezoelectric vibration energy harvester using magnetic force. Int J Mech Sci 2018;135:63–71.

[31] Zhao L, Tang L, Yang Y. Comparison of modeling methods and parametric study for a piezoelectric wind energy harvester. Smart Mater Struct 2013;22:125003.

[32] Erturk A, Inman DJ. An experimentally validated bimorph cantilever model for piezoelectric energy harvesting from base excitations. Smart Mater Struct 2009;18:025009.

[33] Zhou W, Wang B, Lim C, Yang Z. A distributed-parameter electromechanical coupling model for a segmented arc-shaped piezoelectric energy harvester. Mech Syst Signal Process 2021;146:107005.

[34] Hu G, Tang L, Das R, Marzocca P. A two-degree-of-freedom piezoelectric energy harvester with stoppers for achieving enhanced performance. Int J Mech Sci 2018;149:500–7.

[35] Erturk A, Inman DJ. Issues in mathematical modeling of piezoelectric energy harvesters. Smart Mater Struct 2008;17:065016.

[36] Junior CDM, Erturk A, Inman DJ. An electromechanical finite element model for piezoelectric energy harvester plates. J Sound Vib 2009;327:9–25.

[37] Kuang Y, Chew ZJ, Zhu M. Strongly coupled piezoelectric energy harvesters: finite element modelling and experimental validation. Energy Convers Manag 2020;213:112855.

[38] Jo SH, Yoon H, Shin YC, Youn BD. An analytical model of a phononic crystal with a piezoelectric defect for energy harvesting using an electroelastically coupled transfer matrix. Int J Mech Sci 2021;193:106160.

[39] Yang Y, Tang L. Equivalent circuit modeling of piezoelectric energy harvesters. J Intell Mater Syst Struct 2009;20:2223–35.

[40] Fattahi I, Mirdamadi HR. Novel composite finite element model for piezoelectric energy harvesters based on 3D beam kinematics. Compos Struct 2017;179:161–71.

[41] Ramirez JM, Gatti CD, Machado SP, Febbo M. An experimentally validated finite element formulation for modeling 3D rotational energy harvesters. Eng Struct 2017;153:136–45.

[42] Ravi S, Zilian A. Monolithic modeling and finite element analysis of piezoelectric energy harvesters. Acta Mech 2017;228:2251–67.

[43] Wu N, Bao B, Wang Q. Review on engineering structural designs for efficient piezoelectric energy harvesting to obtain high power output. Eng Struct 2021;235:112068.

[44] Sezer N, Koç M. A comprehensive review on the state-of-the-art of piezoelectric energy harvesting. Nano Energy 2021;80:105567.

[45] Sharma A, Kumar R, Vaish R, Chauhan VS. Active vibration control of space antenna reflector over wide temperature range. Compos Struct 2015;128:291–304.

[46] Azadi E, Fazelzadeh SA, Azadi M. Thermally induced vibrations of smart solar panel in a low-orbit satellite. Adv Space Res 2017;59:1502–13.

[47] Li J, Yan S. Thermally induced vibration of composite solar array with honeycomb panels in low earth orbit. Appl Therm Eng 2014;71:419–32.

[48] Bless H, Bohner G, Schwarz N, Strack F. Mood and persuasion: a cognitive response analysis. Pers Soc Psychol Bull 1990;16:331–45.

[49] Liu J, Lu H. Thermal effect on the deformation of a flexible beam with large kinematical driven overall motions. Eur J Mech A Solids 2007;26:137–51.

[50] Daneshjo K, Ramezani M. Classical coupled thermoelasticity in laminated composite plates based on third-order shear deformation theory. Compos Struct 2004;64:369–75.

[51] Khan KA, Muliana AH. Fully coupled heat conduction and deformation analyses of nonlinear viscoelastic composites. Compos Struct 2012;94:2025–37.

[52] Kar A, Kanoria M. Generalized thermoelastic functionally graded orthotropic hollow sphere under thermal shock with three-phase-lag effect. Eur J Mech A Solids 2009;28:757–67.

[53] Wang Y, Zhang X, Song X. A unified generalized thermoelasticity solution for the transient thermal shock problem. Acta Mech 2012;223:735–43.

[54] Liu J, Pan K. Rigid-flexible-thermal coupling dynamic formulation for satellite and plate multibody system. Aerosp Sci Technol 2016;52:102–14.

[55] Liu C, Tian Q, Hu H. Dynamics of a large scale rigid–flexible multibody system composed of composite laminated plates. Multibody Syst Dyn 2011;26:283–305.

[56] Shen Z, Tian Q, Liu X, Hu G. Thermally induced vibrations of flexible beams using absolute nodal coordinate formulation. Aerosp Sci Technol 2013;29:386–93.

[57] Cui Y, Lan P, Zhou H, Yu Z. The rigid-flexible-thermal coupled analysis for spacecraft carrying large-aperture paraboloid antenna. J Comput Nonlinear Dyn 2020;15:031003.

[58] Champier D. Thermoelectric generators: a review of applications. Energy Convers Manag 2017;140:167–81.

[59] Kishore RA, Priya S. A review on low-grade thermal energy harvesting: materials, methods and devices. Materials 2018;11:1433 (Basel).

[60] Thornton EA, Chini GP, Gulik DW. Thermally induced vibrations of a self-shadowed split-blanket solar array. J Spacecr Rocket 1995;32:302–11.

[61] Kim HK, Han CY. Analytical and numerical approaches of a solar array thermal analysis in a low-earth orbit satellite. Adv Space Res 2010;46:1427–39.

[62] Vinyas M, Kattimani SC, Joladarashi S. Hygrothermal coupling analysis of magneto-electroelastic beams using finite element methods. J Therm Stress 2018;41:1063–79.

[63] Dufva K, Shabana A. Analysis of thin plate structures using the absolute nodal coordinate formulation. Proc Inst Mech Eng Part K J Multibody Dyn 2005;219:345–55.

[64] Abbas LK, Rui X, Marzocca P. Aerothermoelastic analysis of panel flutter based on the absolute nodal coordinate formulation. Multibody Syst Dyn 2015;33:163–78.

[65] Shabana AA, Mikkola AM. Use of the finite element absolute nodal coordinate formulation in modeling slope discontinuity. J Mech Des 2003;125:342–50.

[66] Aridogan U, Basdogan I, Erturk A. Analytical modeling and experimental validation of a structurally integrated piezoelectric energy harvester on a thin plate. Smart Mater Struct 2014;23:045039.

[67] De Marqui Junior C, Erturk A, Inman DJ. An electromechanical finite element model for piezoelectric energy harvester plates. J Sound Vib 2009;327:9–25.

[68] Hagood NW, Chung WH, Von Flotow A. Modelling of piezoelectric actuator dynamics for active structural control. J Intell Mater Syst Struct 1990;1:327–54.

[69] Maxam D, Deokar R, Tamma K. A unified computational methodology for dynamic thermoelasticity with multiple subdomains under the GSSSS framework involving differential algebraic equation systems. J Therm Stress 2019;42:163–84.

[70] Masuri S, Sellier M, Zhou X, Tamma K. Design of order-preserving algorithms for transient first-order systems with controllable numerical dissipation. Int J Numer Methods Eng 2011;88:1411–48.

[71] Arnold M, Brüls O. Convergence of the generalized-α scheme for constrained mechanical systems. Multibody Syst Dyn 2007;18:185–202.